

Exploring the mass and redshift dependence of the cluster pressure profile with stacks on thermal SZ maps

DENIS TRAMONTE,^{1,2,3,4,*} YIN-ZHE MA,^{3,4,1,5,†} ZIANG YAN,^{6,7} MATTEO MATURI,^{8,9} GIANLUCA CASTIGNANI,^{10,11}
MAURO SERENO,^{11,12} SANDRO BARDELLI,¹¹ CARLO GIOCOLI,^{11,10,12} FEDERICO MARULLI,^{10,11,12} LAURO MOSCARDINI,^{10,11,12}
EMANUELLA PUDDU,¹³ MARIO RADOVICH,¹⁴ LUDOVIC VAN WAERBEKE,⁷ AND ANGUS H. WRIGHT⁶

¹*Purple Mountain Observatory, No. 8 Yuanhua Road, Qixia District, Nanjing 210034, China*

²*Department of Physics, Xi'an Jiaotong-Liverpool University, 111 Ren'ai Road,*

Suzhou Dushu Lake Science and Education Innovation District, Suzhou Industrial Park, Suzhou 215123, P.R. China

³*NAOC-UKZN Computational Astrophysics Center (NUCAC), University of KwaZulu-Natal, Durban, 4000, South Africa*

⁴*School of Chemistry and Physics, University of KwaZulu-Natal, Westville Campus, Private Bag X54001, Durban, South Africa*

⁵*National Institute for Theoretical and Computational Sciences (NITheCS), South Africa*

⁶*Ruhr University Bochum, Faculty of Physics and Astronomy, Astronomical Institute (AIRUB), German Centre for Cosmological Lensing, 44780 Bochum, Germany*

⁷*Department of Physics and Astronomy, University of British Columbia, 6224 Agricultural Road, Vancouver, BC, V6T 1Z1, Canada*

⁸*Center for Astronomy - University of Heidelberg, Albert-Ueberle-Straße 2, 69120 Heidelberg, Germany*

⁹*Institute of Theoretical Physics - University of Heidelberg, Albert-Ueberle-Straße 2, 69120 Heidelberg, Germany*

¹⁰*Department of Physics and Astronomy "A. Righi" - Alma Mater Studiorum University of Bologna, Via Piero Gobetti 93/2, 40129 Bologna, Italy*

¹¹*INAF - Astrophysics and Space Science Observatory of Bologna, Via Piero Gobetti 93/3, 40129 Bologna, Italy*

¹²*INFN - Bologna Section, Viale Bertini Pichat 6/2, 40127 Bologna, Italy*

¹³*INAF - Osservatorio Astronomico di Capodimonte, Salita Moiariello 16, I-80131, Napoli, Italy*

¹⁴*INAF - Padua Astronomical Observatory, Vicolo dell'Osservatorio, 5, 35122 Padova, Italy*

(Received September 9, 2022; Revised December 12, 2022; Accepted February 11, 2023)

Submitted to ApJS

ABSTRACT

We provide novel constraints on the parameters defining the universal pressure profile (UPP) within clusters of galaxies, and explore their dependence on the cluster mass and redshift, from measurements of Sunyaev-Zel'dovich Compton- y profiles. We employ both the *Planck* 2015 MILCA and the ACT-DR4 y maps over the common $\sim 2,100$ deg² footprint. We combine existing cluster catalogs based on KiDS, SDSS and DESI observations, for a total of 23,820 clusters spanning the mass range $10^{14.0} M_{\odot} < M_{500} < 10^{15.1} M_{\odot}$ and the redshift range $0.02 < z < 0.98$. We split the clusters into three independent bins in mass and redshift; for each combination we detect the stacked SZ cluster signal and extract the mean y angular profile. The latter is predicted theoretically adopting a halo model framework, and MCMCs are employed to estimate the UPP parameters, the hydrostatic mass bias b_h and possible cluster miscentering effects. We constrain $[P_0, c_{500}, \alpha, \beta]$ to $[5.9, 2.0, 1.8, 4.9]$ with *Planck* and to $[3.8, 1.3, 1.0, 4.4]$ with ACT using the full cluster sample, in agreement with previous findings. We do not find any compelling evidence for a residual mass or redshift dependence, thus expanding the validity of the cluster pressure profile over much larger M_{500} and z ranges; this is the first time the model has been tested on such a large (complete and representative) cluster sample. Finally, we obtain loose constraints on the hydrostatic mass bias in the range 0.2-0.3, again in broad agreement with previous works.

Keywords: galaxies: clusters: general — galaxies: clusters: intracluster medium — large-scale structure of universe

1. INTRODUCTION

Galaxy clusters are an invaluable cosmological probe, providing information on the geometry of the Universe, on the growth of cosmic structures, and, at lower scales, on the processes of galaxy formation and evolution (Voit 2005; Allen et al. 2011). The majority of cluster baryonic matter (up to 90%) is found as a diffuse component referred to as the intra-cluster medium (ICM), which is shock-heated and ionized in the strong cluster gravitational field, up to temperatures of 5-10 keV. A proper characterization of the ICM physical properties is of great interest, not only for allowing an indirect calibration of the mass proxies based on ICM observations, but also for providing useful insights in the processes of galaxy evolution and feedback.

The high temperature of the ICM plasma has made it a traditional target for X-ray observations (Sarazin 1988), a property that has been exploited by different generations of satellite missions to build X-ray cluster catalogs (Voges et al. 1999; Hicks et al. 2008; Mehrrens et al. 2012; Klein et al. 2021). A complementary probe is the observation of the thermal Sunyaev-Zel'dovich (tSZ) effect (Sunyaev & Zeldovich 1972), a secondary anisotropy of the cosmic microwave background (CMB) radiation which is produced when CMB photons interact with a population of high-energy electrons via inverse Compton scattering. The resulting temperature fluctuations with respect to the CMB temperature T_{CMB} can be expressed as:

$$\frac{\Delta T}{T_{\text{CMB}}} = f(\xi)y, \quad (1)$$

where the dependence on the scaled frequency $\xi \equiv h\nu/(k_{\text{B}}T_{\text{CMB}})$, h and k_{B} being the Planck and Boltzmann constants, is encoded in the function $f(\xi) = \xi \coth(\xi/2) - 4$; the result is a decrease (increase) of the CMB temperature at frequencies below (above) 217 GHz. The magnitude of the effect is quantified by the Compton parameter y which is proportional to the electron pressure integrated along the line of sight (LoS):

$$y = \frac{\sigma_{\text{T}}}{m_{\text{e}}c^2} \int_{\text{LoS}} dl P_{\text{e}}(l), \quad (2)$$

where σ_{T} is the Thomson cross-section, $m_{\text{e}}c^2$ the electron rest energy and $P_{\text{e}}(l)$ the electron pressure at a physical LoS separation l .

The high energy electrons found in the ICM make the tSZ effect an ideal probe to detect and study galaxy

clusters (Birkinshaw 1999; Carlstrom et al. 2002). Unlike the X-ray brightness, which is proportional to the squared electron density n_{e}^2 , the Compton parameter is proportional to n_{e} , which implies that it has a higher sensitivity to low mass densities and can be used to trace the ICM out to larger separations from the cluster core. In addition, it is independent of the cluster redshift¹, and tSZ observations can be conveniently carried out at radio and microwave frequencies from ground-based observatories. The advances in tSZ observational techniques during the past two decades have yielded dedicated tSZ-detected cluster catalogs and the reconstruction of the Compton parameter signal over extended areas of the sky, using both satellite missions like *Planck* (Planck Collaboration et al. 2016a) and ground-based facilities like the Atacama Cosmology Telescope (ACT, Hilton et al. 2021) and the South Pole Telescope (SPT, Bleem et al. 2020).

Both in the case of X-ray or tSZ data, a proper characterization of the ICM eventually translates into the modeling of the local electron pressure. The analysis presented in Nagai et al. (2007) first proposed a generalized Navarro-Frenk-White (NFW, Navarro et al. 1997) parametrization as a universal model for the electron pressure profile, in the form:

$$\begin{aligned} \mathbb{P}(x) &\equiv \frac{P_{\text{e}}(r)}{P_{500}} \\ &= \frac{P_0}{(c_{500}x)^\gamma [1 + (c_{500}x)^\alpha]^{(\beta-\gamma)/\alpha}}, \end{aligned} \quad (3)$$

where $P_{\text{e}}(r)$ is the electron pressure at a physical separation r from the cluster center, P_{500} is the characteristic pressure expected in a self-similar model (Section 5.1), carrying the dependence on the cluster mass and redshift, and the profile is expressed as a function of the scaled radial separation² $x \equiv r/R_{500}$. This universal pressure profile (hereafter UPP) is parametrized in terms of the concentration³ c_{500} , an overall normaliza-

¹ Strictly speaking, tSZ observations detect the cluster signal integrated over the beam solid angle Y_{SZ} , which is proportional to the temperature-weighted mass of the cluster $M\langle T_{\text{e}} \rangle$ and to the inverse square of the angular diameter distance at the cluster redshift, $Y_{\text{SZ}} \propto M\langle T_{\text{e}} \rangle D_{\text{A}}(z)^{-2}$ (Carlstrom et al. 2002). This introduces a marginal redshift dependence. In fact, tSZ detections of clusters at $z > 1$ are not common, possibly due to a lower ICM temperature or the contamination from radio loud AGNs.

² Unless explicitly stated, it is understood that overdensity masses and radii are referred to the Universe critical density $\rho_{\text{c}}(z)$ at the considered redshift; in formulae, $M_{\Delta} = 4\pi\Delta\rho_{\text{c}}(z)R_{\Delta}^3/3$, with Δ the overdensity value.

³ In some work, the UPP is expressed as a function of $x' = r/r_{\text{s}}$, where the scale radius r_{s} is related to the overdensity radius R_{500} via the concentration parameter, $c_{500} = R_{500}/r_{\text{s}}$.

* D. Tramonte, Denis.Tramonte@xjtlu.edu.cn

† Y.-Z. Ma, ma@ukzn.ac.za

Table 1. Summary of previous estimates on the parameters entering the UPP expression in equation (3). For each work we report the reference in the literature, the number of clusters used in the study (when applicable), the used physical observables and the best-fit values for the UPP parameters. Boldface values were kept fixed in the corresponding fit. For more details we redirect to Appendix A.

Reference	Data set		UPP parameters				
	Objects	Observables	P_0	c_{500}	α	β	γ
Nagai et al. (2007)	16 clusters	X-ray, simulations	3.3	1.8	1.3	4.3	0.7
Arnaud et al. (2010)	33 clusters	X-ray, simulations	$8.403 h_{70}^{-3/2}$	1.177	1.0510	5.4905	0.3081
Planck Collaboration et al. (2013)	62 clusters	SZ, X-ray	6.41	1.81	1.33	4.13	0.31
Sayers et al. (2016)	47 clusters	SZ, X-ray	9.13 ± 2.98	1.18	1.0510	6.13 ± 0.76	0.3081
Gong et al. (2019)	$\sim 10^5$ LRGs	SZ	$2.18^{+9.02}_{-1.98}$	$1.05^{+1.27}_{-0.47}$	$1.52^{+1.47}_{-0.58}$	$3.91^{+0.87}_{-0.44}$	0.31
Ma et al. (2021)	-	SZ, WL (convergence)	$9.68^{+10.02}_{-7.11}$	$2.71^{+0.92}_{-0.93}$	$5.97^{+1.81}_{-4.73}$	$3.47^{+1.39}_{-0.60}$	0.31
Ma et al. (2021)	-	SZ, WL (shear)	$6.62^{+2.06}_{-1.65}$	$1.91^{+1.07}_{-0.65}$	$1.65^{+0.74}_{-0.50}$	$4.88^{+1.18}_{-2.46}$	0.31
Pointecouteau et al. (2021)	31 clusters	SZ	$3.36^{+0.90}_{-0.71}$	1.18	$1.08^{+0.13}_{-0.11}$	4.30 ± 0.12	0.31
He et al. (2021)	33 clusters	X-ray, simulations	5.048	1.217	1.192	5.490	0.433

tion factor P_0 , and the parameters γ , α and β which are, respectively, the profile slopes at small ($x \ll 1/c_{500}$), intermediate ($x \sim 1/c_{500}$) and large ($x \gg 1/c_{500}$) separations from the cluster center. Nagai et al. (2007) provided best-fit estimates for the parameters based on profiles reconstructed from *Chandra* data and results from hydrodynamical simulations.

In the past decade, several other works have contributed to constraining the UPP parameters using different observables and techniques. A summary of the results on the fitted UPP parameters from these works is reported in Table 1, while for a more comprehensive summary we redirect to Appendix A. Most of these studies employed a limited set of well-characterized and high-significance clusters to measure the cluster pressure profile (Arnaud et al. 2010; Planck Collaboration et al. 2013; Sayers et al. 2016; Pointecouteau et al. 2021; He et al. 2021). A substantially different approach was instead adopted in Gong et al. (2019), hereafter G19, where the UPP parameters were fitted over the stack of a large number ($\sim 10^5$) of regions surrounding luminous red galaxies (LRGs) at $z \lesssim 0.5$, assuming the latter are good tracers of massive dark matter halos. This type of work foregoes the profile reconstruction for individual objects and focuses instead on the mean ICM properties of an extended sample. The results were in agreement with previous studies, thus proving the feasibility of this

approach for characterizing the UPP. Besides, the large number statistics provided by the sample in G19 allowed the authors to split the LRG sample into three redshift bins, finding hints of a redshift evolution of the UPP parameters; the inclusion of an explicit redshift dependence in the normalization pressure P_{500} proved effective in improving the reduced χ^2 when fitting the combination of the three redshift bins. Finally, other, more indirect estimates of the UPP parameters were obtained from the cross-correlation between tSZ and weak lensing (WL) data (Hojjati et al. 2015, 2017; Ma et al. 2021).

The present study aims at extending this line of work by providing novel estimates of the UPP parameters. Our analysis is based on cluster stacks on y maps; the UPP parameters are then fitted on the reconstructed mean y profiles. The main difference with G19 is that we will use a real cluster catalog instead of reverting to LRGs as positional tracers. Besides, we will be using a *complete* cluster sample; this is a major difference compared to the cluster-based studies listed in Table 1, whose high-significance cluster samples were non-complete and in some cases even non-representative (see Appendix A for a more extensive discussion). Our sample is obtained by merging existing cluster catalogs, yielding a total of $\sim 2.3 \times 10^4$ clusters spanning the M_{500} mass range $[10^{14}, 10^{15.1}] M_\odot$ and the photometric redshift range $[0.1, 0.8]$. This is another important differ-

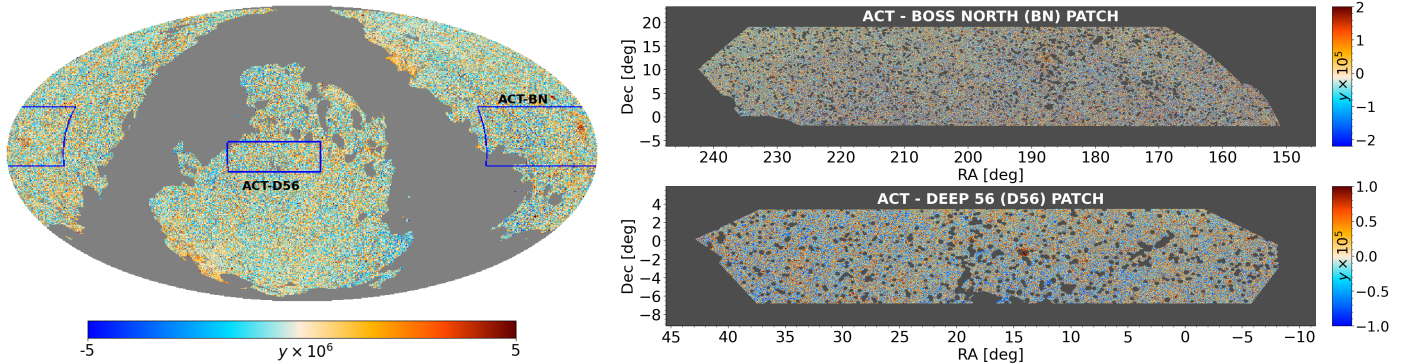


Figure 1. *Left:* the all-sky *Planck* 2015 MILCA Compton y -map, plotted in equatorial coordinates with the Galactic plane 40% mask and the point source mask overlapped; the position of the two ACT patches is also marked with blue boxes. *Right:* the two patches of the ACT-DR4 y -map, combined with the local projection of the mask adopted for *Planck*. The color scale units are different in *Planck* and ACT to better show the features in the corresponding maps; in both cases, masked regions are shown in gray color.

ence compared with the analysis in G19, which targeted mostly the mass range of rich groups ($M_{500} \lesssim 10^{14} M_{\odot}$). Furthermore, our large sample allows us to split the data set not only in different redshift bins but also in different mass bins, thus exploring in more detail possible deviations from the universality of the pressure profile. Finally, we will obtain independent results from both *Planck* and ACT Compton maps for the same cluster sample.

This paper is organized as follows. We begin by describing the two data sets employed in our analysis, namely the Compton y -maps (Section 2) and the cluster catalogs (Section 3). Section 4 presents the methodology we adopt for generating our reference sample, stacking the clusters, and extracting the associated angular y profiles with their uncertainties. The formalism we employ to model the cluster y signal is detailed in Section 5, whereas the parameter estimation analysis is presented in Section 6. Finally, Section 7 reports the conclusions. Throughout this paper we adopt a spatially-flat Λ CDM cosmological model with parameter values $h = 0.674$, $\Omega_m = 0.315$, $\Omega_b = 0.0493$, $\sigma_8 = 0.811$ and $n_s = 0.965$ (Planck Collaboration et al. 2020).

2. COMPTON PARAMETER MAPS

In this work we conduct the stacking analysis on two different Compton parameter maps, obtained by *Planck* and ACT. We describe each in details in the following.

2.1. *Planck* data

We employ the all-sky Compton parameter map delivered by the *Planck* Collaboration and described in Planck Collaboration et al. (2016b). The map is

publicly available at the *Planck* Legacy Archive⁴, and can be downloaded in HEALPix format (Górski et al. 2005) with a pixelization set by the resolution parameter $N_{\text{side}} = 2048$ (corresponding to a pixel size of ~ 1.8 arcmin). The map was generated via a tailored linear combination of *Planck* individual frequency maps. Two versions of the map are available, obtained from two different implementations of the Internal Linear Combination (ILC) algorithm, namely the Modified Internal Linear Combination Algorithm (MILCA, Hurier et al. 2013) and the Needlet Independent Linear Combination (NILC, Remazeilles et al. 2011) method. In the following we will adopt the MILCA map only, as we verified that the use of the NILC map yields results on the Compton parameter profiles compatible within the final error bars. Prior to their linear combination, *Planck* channel maps were first degraded to a common resolution of 10 arcmin, which is the reference full-width at half maximum (FWHM) value for the final Compton map.

We adopt a suitable mask to avoid contamination from residual Galactic foregrounds and strong extragalactic radio sources. The *Planck* Legacy Archive provides a point source mask and different Galactic masks tailored to the tSZ analysis. We combine the 40% Galactic plane mask and the point source mask, excluding a total 50.6% of the sky. The *Planck* MILCA Compton map, combined with our adopted mask, is shown in the first panel of Fig. 1.

2.2. ACT data

We employ the ACT Compton y -map described in Madhavacheril et al. (2020) and publicly accessible

⁴ <https://pla.esac.esa.int/#maps>.

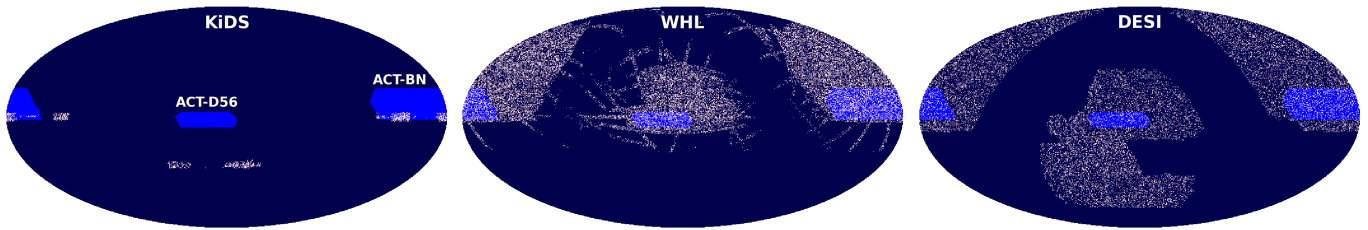


Figure 2. Footprint of the two ACT patches (lighter blue) adopting the same equatorial frame as in the first panel of Fig. 1, compared with the angular distribution of our chosen cluster catalogs (white color), namely KiDS (left), WHL (middle) and DESI (right).

at the LAMBDA website⁵. This map was also built with an ILC approach using *Planck* individual frequency maps⁶ up to 545 GHz and ACT maps at 98 and 150 GHz. The two experiments are complementary in terms of angular sensitivity: whereas ACT has higher resolution than *Planck* and provides superior quality data at small scales, *Planck* large-scale data are free from the atmospheric noise affecting ACT maps. The limited available sky area of $\sim 2,100 \text{ deg}^2$ allowed the authors to apply an ILC implementation tailored to a projected 2-dimensional analysis, which is a novel approach compared to previous spherical harmonics-based approaches to analyze all-sky data. The final map covers two disjoint patches in the sky, labelled as BOSS North (BN, covering $1,633 \text{ deg}^2$) and Deep 56 (D56, covering 456 deg^2), where deep observational ACT data from 2014 and 2015 were available. Unlike *Planck* maps, ACT maps for these patches are provided as two-dimensional arrays in a *plate carrée* (equirectangular) projection, with a pixel size of ~ 0.5 arcmin. The resolution of these ACT maps is $\text{FWHM} = 1.6$ arcmin.

Although individual frequency maps underwent a process of source subtraction prior to their combination, possible residuals are still present in the final product. As no specific point-source mask is available for ACT tSZ maps, we revert to using the same combined Galactic and point source *Planck* mask also for these maps,

⁵ https://lambda.gsfc.nasa.gov/product/act/act_dr4_derived_maps_get.cfm.

⁶ Hence, *Planck* and ACT tSZ maps are not completely independent. This, however, is not an issue in our study, as the choice of using both data sets has been made to better exploit all the available tSZ data. In the end, the higher resolution of ACT is still the main factor making a difference in the resulting angular Compton profiles.

by projecting it on the plane areas covered by ACT⁷. The resulting masked maps are plotted in the two right panels of Fig. 1.

3. CLUSTER CATALOGS

We consider a composite cluster sample obtained by merging three independent catalogs, described individually in the following. The methodology we adopt for their combination is addressed in Sections 3.4 and 3.5. Notice that in the end we will only consider clusters with mass $M_{500} > 10^{14} M_{\odot}$, as lower masses would not yield a significant detection in the stacks described in Section 4.2.

3.1. AMICO-KiDS DR3 Catalog

We employ the cluster catalog described in Maturi et al. (2019), which was obtained by running the Adaptive Matched Identifier of Clustered Objects (AMICO) algorithm (Bellagamba et al. 2018) on the third data release of the Kilo Degree Survey (KiDS-DR3, de Jong et al. 2017). KiDS-DR3 data provide photometric redshifts for ~ 48.7 million sources over 447 deg^2 . AMICO is based on a linear optimal matched filter which (in this particular application) exploits information on galaxy positions, r -band magnitude, and redshift distribution to build a three-dimensional map of the amplitude A over the volume spanned by the galaxy catalog. The quantity A , which is evaluated with its associated variance σ_A , is related to the likelihood of finding a galaxy cluster; the location with the highest likelihood is then identified as the first cluster candidate. The signal associated with the latter is subsequently removed from the A map, before re-evaluating the likelihood and searching for the second cluster candidate. The pro-

⁷ Although this mask may potentially miss some point sources entering the ACT footprint, it can be considered conservative as the larger *Planck* beam size would result in a larger masked area around each compact source. We also explicitly tested that the use of no mask at all produces negligible variations in the ACT profiles presented in Section 10, thus proving that the specific masking strategy is not a critical issue in a stacking analysis like the one presented in this paper.

cess is repeated until reaching a low-limit signal-to-noise (S/N) ratio $A/\sigma_A = 3$; the final output catalog contains 12,939 clusters identified with $S/N > 3$, over the redshift range $0.078 < z < 0.754$. We restrict our analysis to the 7,957 clusters with $S/N > 3.5$; the resulting sample has a typical $\gtrsim 95\%$ purity over the whole redshift range and a completeness $\gtrsim 90\%$ for $M_{500} > 10^{14} M_\odot$ at $z < 0.6$ (Maturi et al. 2019).

The measured amplitude A served as the primary mass proxy for each detection; cluster masses were assigned on the basis of an $A-M_{200}$ scaling relation, where the baseline mean values for the overdensity mass M_{200} were computed from KiDS lensing data (Bellagamba et al. 2019). As it is customary to employ M_{500} as the mass definition in tSZ studies, we convert the AMICO masses into M_{500} assuming a NFW profile and using the concentration model from Ishiyama et al. (2021). For each cluster we also generate a population of 200 random values of masses, normally distributed around the M_{200} value and with a dispersion set by the available uncertainty $\sigma_{M_{200}}$; we convert each of these values to M_{500} and adopt their root mean square (*rms*) as our estimate for the uncertainty $\sigma_{M_{500}}$. The resulting, mean uncertainty on $\log_{10}(M_{500}/M_\odot)$ for KiDS clusters is 0.194 dex. When queried to match the ACT footprint, the KiDS catalog contributes with 3,318 clusters (806 clusters with $M_{500} > 10^{14} M_\odot$), all located in the ACT-BN patch (Fig. 2, left panel).

3.2. SDSS-DR12 WHL Catalog

The catalog described in Wen et al. (2012) identified 132,684 galaxy clusters based on SDSS-DR8 (Aihara et al. 2011) photometric data in the redshift range $0.05 \leq z < 0.80$. The catalog has a $\gtrsim 94\%$ purity over the whole sample and a $\gtrsim 95\%$ completeness for clusters with $M_{200} > 10^{14} M_\odot$ at $z < 0.42$; cluster masses were estimated based on their richness and optical luminosity. A more recent update of the catalog, based on SDSS-DR12 (Alam et al. 2015), is presented in Wen & Han (2015); hereafter we shall label such catalog as WHL⁸. The update not only took advantage of the improved SDSS data quality, which provided additional spectroscopic redshift information for a total of ~ 2.3 million galaxies and allowed to improve cluster detection at high redshifts, but also exploited a better-defined mass proxy. The new catalog includes 25,419 additional clusters detected around bright galaxies at high redshift

and provides updated redshift and richness estimates for the previously identified objects. Each cluster position is defined by the coordinates of its brightest cluster galaxy (BCG), and its redshift is estimated as the mean of the spectroscopic redshifts of member galaxies (when available). As for the mass estimation, the analysis firstly defined a calibration sample by merging existing cluster samples with mass proxies based on X-ray data (Vikhlinin et al. 2009; Mantz et al. 2010; Piffaretti et al. 2011; Takey et al. 2014) or tSZ-data (Hasselfield et al. 2013; Planck Collaboration et al. 2016a). Common clusters across different catalogs were used to yield a homogeneous mass definition throughout the composite sample, by scaling it to the definition adopted in Vikhlinin et al. (2009). The final calibration sample consisted of 1191 clusters overlapping with available SDSS data, with mass⁹ $M_{500} > 0.3 \times 10^{14} M_\odot$ and redshift $0.05 < z < 0.75$. For these clusters, the total r -band luminosity within R_{500} , corrected by a redshift-dependent factor, was found to be well correlated with the cluster mass M_{500} with a scatter of 0.17 dex. The associated scaling relation can be applied to estimate the mass of all clusters in the updated WHL catalog.

For our analysis, we employ the updated WHL catalog with a total of 158,103 clusters spanning the mass range $M_{500} \in [10^{12.3}, 10^{15.5}] M_\odot$ and the redshift range $[0.03, 0.80]$, about 77% of which with spectroscopic redshift information. As there is no mass error estimate available for individual clusters, we evaluate a mean uncertainty on M_{500} as follows. We consider clusters in the calibration sample and convert their measured richness into mass $M_{500}^{(\text{scal})}$, adopting the same scaling relation that was employed in Wen & Han (2015) to compute the mass estimates for the updated cluster catalog. For the calibration sample clusters, the independent mass estimate $M_{500}^{(\text{lit})}$ from the literature is also available¹⁰; we consider then the scatter values $M_{500}^{(\text{scal})} - M_{500}^{(\text{lit})}$ for the calibration clusters and take their *rms* as the common mass uncertainty for the WHL catalog we use in our analysis. The result is an uncertainty of 0.187 dex in $\log_{10}(M_{500}/M_\odot)$, which is slightly more conservative than the value quoted for the scatter of the scaling relation in Wen & Han (2015). The query for matching the ACT footprints yields 27,367 clusters, of which 20,967 in the BN patch and 6,400 in the D56 patch (Fig. 2, central

⁸ This acronym contains the initials of the authors of the original publication (Wen et al. 2012). The catalog is publicly available at <https://vizier.u-strasbg.fr/viz-bin/VizieR?-source=J/ApJ/807/178>.

⁹ Unlike Wen et al. (2012), where masses are quoted as M_{200} , the work in Wen & Han (2015) adopts the M_{500} definition.

¹⁰ These mass estimates $M_{500}^{(\text{lit})}$ are the ones obtained from the aforementioned list of X-ray and tSZ studies, after the rescaling performed by Wen & Han (2015) to homogenize the mass definition in the calibration sample.

panel); after applying the mass cut $M_{500} > 10^{14} M_{\odot}$, the numbers are 18,597, 14,186 and 4,411, respectively.

3.3. DESI-DR8 Catalog

This cluster catalog was obtained directly from galaxy samples in the DESI Legacy Imaging Surveys (Dey et al. 2019) Data Release 8 (DESI-DR8 hereafter). The catalog production is described in Yang et al. (2021) and is based on the updated version of the halo-based group/cluster finder presented in Yang et al. (2005) and later employed in Yang et al. (2007). In this case, the cluster mass is computed based on the measured cluster luminosity. The group finder follows an iterative approach: at each stage, the cumulative group luminosity distribution is computed from the known luminosity of member galaxies; abundance matching with the cumulative halo mass function allows assigning to each group a tentative mass, which in turn allows the update of the membership information. The process starts by assuming that each galaxy is a group candidate, and continues until convergence in the galaxy membership information and in the derived mass-to-luminosity ratios. In this case, the estimated mass is defined for an overdensity $\Delta = 180$ with respect to the mean matter density of the Universe at the cluster redshift ($M_{180,m}$), and the cluster position is assigned to its geometrical, luminosity-weighted center. The authors first tested this halo finder on a mock galaxy catalog generated from the ELUCID simulation (Wang et al. 2016), comparing the results with the output of a traditional Friend-of-Friends algorithm (Davis et al. 1985): in $\sim 90\%$ of groups with mass $M_{180,m} \gtrsim 10^{12.5} h^{-1} M_{\odot}$, the halo finder correctly identified more than 60% of the member galaxies, with a quoted mean mass uncertainty of 0.2 dex for masses $M_{180,m} \gtrsim 10^{13.5} h^{-1} M_{\odot}$; the purity resulted $> 90\%$ for groups with mass $M_{180,m} \gtrsim 10^{12} h^{-1} M_{\odot}$ and reached $\sim 100\%$ for $M_{180,m} \gtrsim 10^{14.5} h^{-1} M_{\odot}$.

The authors subsequently applied the group finder to DESI-DR8 to yield positions, redshifts and masses for ~ 92 million objects, the majority of which being low mass groups with less than 3 member galaxies. For the purpose of the present analysis we clearly restrict the sample to the most massive objects; after converting the mass to the M_{500} definition with the concentration model from Ishiyama et al. (2021), we apply the mass cut $M_{500} > 10^{14} M_{\odot}$, resulting in a total of 110,908 objects spanning the redshift range $z \in [0.02, 0.97]$. Given our lower mass cut, and the lack of error estimates on individual cluster masses, we can adopt the quoted value 0.2 dex as the common uncertainty on $\log_{10}(M_{500}/M_{\odot})$. We find 13,018 clusters overlapping with ACT maps,

10,253 in the BN patch and 2,765 in the D56 patch (Fig. 2, right panel).

3.4. Mass calibration

With the aim of employing the largest possible statistics in our study of the cluster pressure profile, we merge together the three catalogs described above. In order to avoid potential biases in the subsequent analysis, care needs to be taken in this operation to ensure that the cluster mass definition is consistent across all catalogs we will combine. Although in every case we adopt the M_{500} definition, masses from different catalogs are based on different observables, scaling relations and methodologies.

We then search for cluster matches between pairs of catalogs, and compare the associated mass values. Our matching criterion is purely positional: two clusters in different catalogs are considered to be the same object if their projected linear separation on the sky Δr and their redshift separation Δz satisfy the conditions $\Delta r < 0.5$ Mpc and $\Delta z < 0.05(1 + \bar{z})$, where \bar{z} is the mean redshift of the two clusters (this expression for the limit in Δz takes into account the possible higher errors on z measurements at higher redshifts). This query is applied to the full catalogs (not restricted to the ACT footprint), but keeping the constraint $M_{500} > 10^{14} M_{\odot}$. Besides, the search for matches is conducted in four disjoint redshift intervals, namely $[0.00, 0.35]$, $[0.35, 0.45]$, $[0.45, 0.55]$, $[0.55, 0.80]$; the different interval size takes into account the non-uniform redshift distributions of our cluster catalogs, and allows to yield a comparable number of matches in each bin. The reason why we perform this analysis in different redshift bins is to allow for a possible z evolution in the agreement of the mass estimates from different catalogs. The number of chosen redshift bins is rather arbitrary; in our case, 4 bins are enough to show any redshift trend while retaining a number of matches per bin which is large enough for the subsequent analysis.

The results of the query for cluster matches are shown in the left panels of Figs. 3, 4 and 5 for the combinations KiDS-WHL, KiDS-DESI and WHL-DESI respectively. Each plot refers to one redshift interval and shows the comparison between the masses of the matched clusters as obtained from the corresponding catalogs, together with the bisector $y = x$ that represents the ideal case of equality. In order to avoid excessive clutter in these plots, the mean error bars associated with the mass estimates are shown in a separate box in each top-left corner. We typically find around 100 cluster matches per redshift bin when considering the KiDS catalog, and typically more than 7000 matches for the combination of the

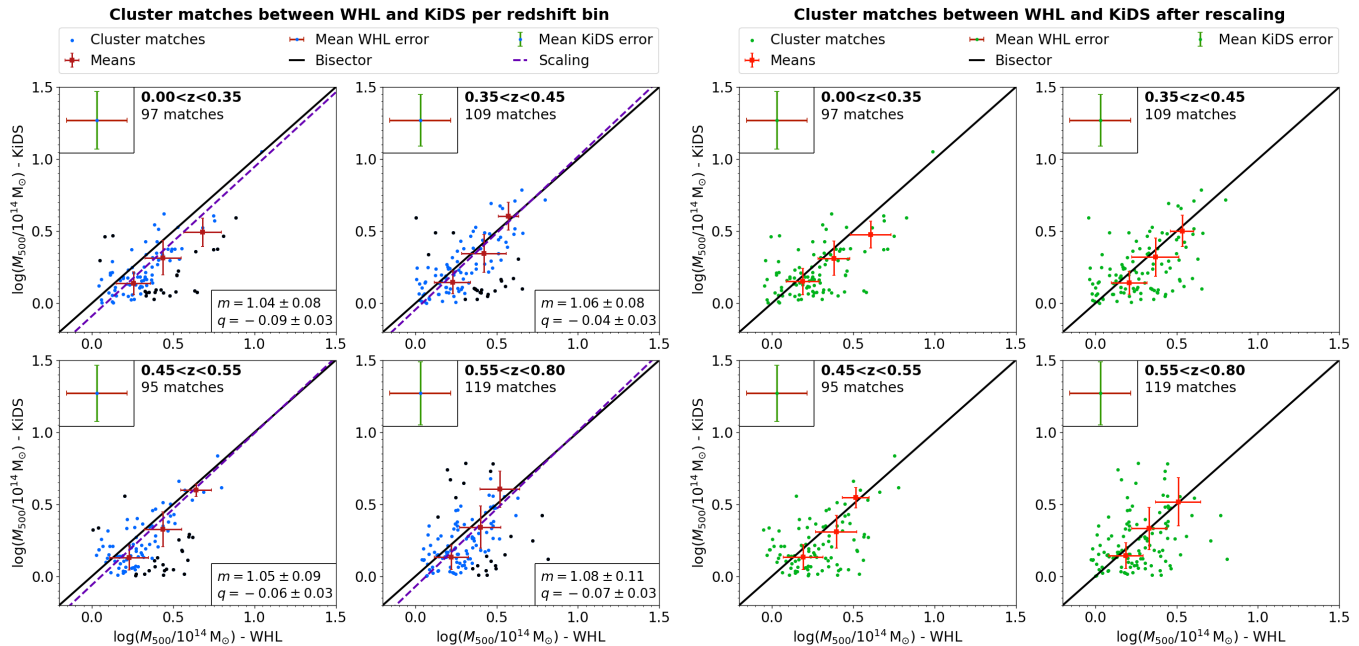


Figure 3. Summary of the mass calibration analysis described in Section 3.4, for the case of KiDS-WHL comparison. *Left panels:* for each redshift bin, we plot a comparison between masses from the two catalogs for the retrieved cluster matches using dots; the bisector $y = x$ is shown for comparison as a solid black line. The mean error bars for the mass estimates of each match are shown in a separate box in the top-left corner. The red squares and their error bars represent the mean and standard deviation for the masses of matches binned along the bisector, and serve to better visualize the trend of the points compared to the bisector. The purple dashed line represents the linear regression adopted to scale WHL masses to KiDS masses according to Eq. (4), with the scaling parameters quoted in the low-right corner of each plot; matches plotted in black were considered outliers and not included in the linear fit. *Right panels:* same as for the left panels, but after applying the rescaling to WHL masses; the scaling overall improves the agreement between the masses of matched clusters.

larger catalogs WHL and DESI. In all plots the masses are quoted in logarithmic units of $10^{14} M_{\odot}$, which is a convenient choice as it sets our low mass threshold at the origin.

As expected, the intrinsic scatter of the scaling relations adopted to estimate each cluster mass, combined with the uncertainty in the measurement of the associated mass proxy, determines a visible scatter of the points around the bisector. However, if the distribution of points also shows any clear trend deviating from the bisector, the mass estimates we are adopting could be systematically biased. This effect is better visualized by splitting the points into different mass bins and just considering the associated mean masses computed for each catalog. In principle, the bins could be defined along each of the two coordinate axes, by choosing the corresponding catalog as a reference. In this case, however, the mass estimates from all catalogs have significant error bars, which makes this strategy for splitting the points unreliable. In order not to make a preferential choice for any catalog, we group instead the points in bins of equal separation from the line $y = -x$, or in other words, we bin the points along the bisector, with the boundaries for each bin being the lines $y = -x + \Delta$

(with $\Delta \simeq 0.2$). In Figs. 3 to 5 the mean masses of the points in each bin are shown as red squares, while their standard deviations are quantified by the associated error bars.

In general, considering the mass uncertainties shown in the top left corner of each plot, individual matches are compatible with the bisector within 1σ ; the mean points, however, reveal in some cases a trend or an offset that deviates from the bisector. It is then meaningful to correct for this effect following the procedure adopted in Wen & Han (2015), where the same issue was encountered when building the calibration cluster sample by merging pre-existing independent catalogs. We then choose a reference catalog for the mass definition and re-scale the masses of the other two catalogs to match the values from the reference one. Masses for the KiDS clusters are obtained via a richness-mass scaling relation calibrated on weak lensing measurements, which directly probe the cluster mass without any assumption on their physical state; hence, they can be considered more reliable than the masses quoted in WHL, which rely on the tSZ and X-ray masses defined in the calibration sample, or in DESI, which relies on the abundance matching between halo luminosity and mass function.

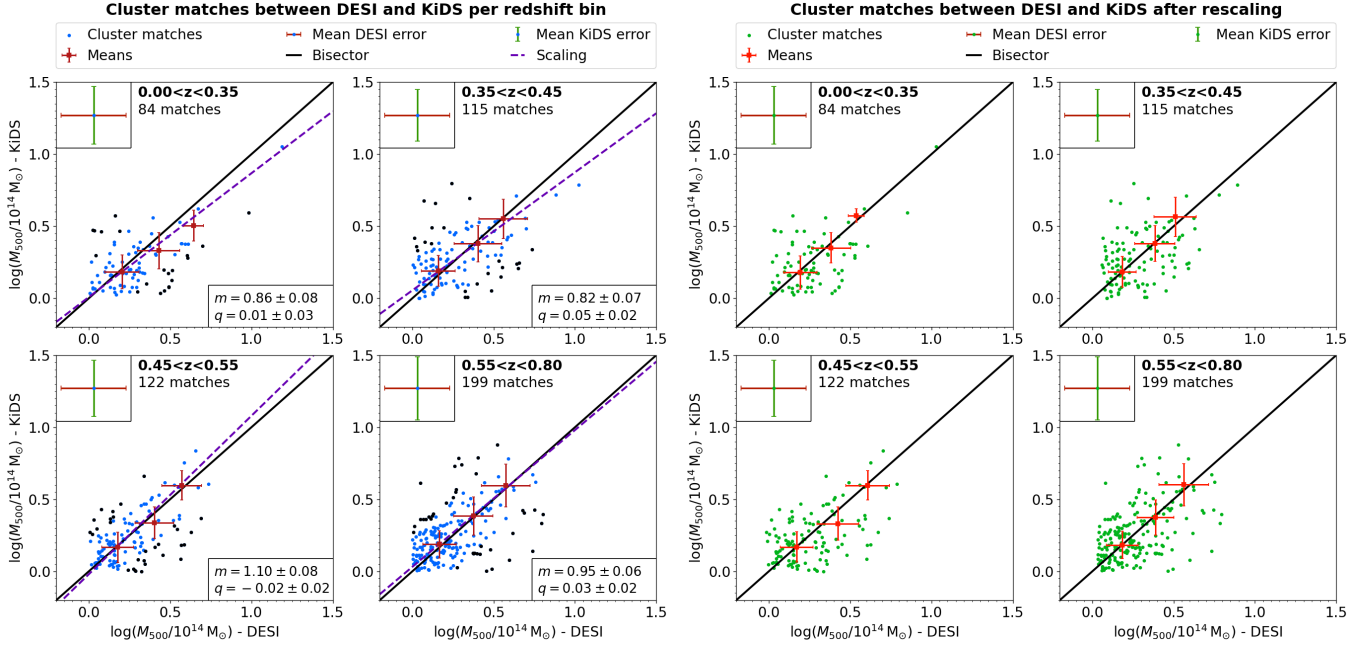


Figure 4. Same as in Fig. 3, but for the comparison between KiDS and DESI.

We shall therefore take KiDS as the reference catalog, and scale the masses in the other catalogs accordingly. For each redshift bin the scaling has the form:

$$\log_{10} \tilde{M}_{\text{KiDS}} = m_{X,i} \log_{10} \tilde{M}_X + q_{X,i}, \quad (4)$$

where $\tilde{M} \equiv M/(10^{14} M_\odot)$, X is either WHL or DESI, i selects the redshift bin, and the parameters m and q are obtained via linear regression on the masses of the associated matches.

In this context results from the linear regression can easily be biased by outliers. The latter could be a result of spurious matches, or of the combination of the intrinsic scatters in the scaling relations adopted to derive the cluster mass in the two catalogs (combined with the uncertainties in the measurements of the mass proxies themselves). In order for our fits not to be biased by these outliers, we identify and remove them according to the following procedure. In each of the mass bins bounded by the $y = -x + \Delta$ edge lines, we compute the orthogonal distance d of each point to the bisector, and evaluate the associated standard deviation σ_d ; for each bin, we then discard all points for which $d > 2\sigma_d$ from the linear regression analysis. These outliers are shown in black color in the left panels of Figs. 3, 4 and 5. For the remaining points, due to the large error bars in both axes, an ordinary least square fit would not be suitable in our case; we adopt instead an orthogonal distance regression method using the SciPy ODR package¹¹. The

resulting linear scalings are plotted as dashed purple lines in Figs. 3 and 4, where a box in each low-right corner reports the best-fit parameters. We notice that in all cases the intercept satisfies $|q| < 0.1$; this result already suggests a broad consistency between mass estimates from different catalogs, as in the ideal case of $m = 1$ the intercept quantifies the mean offset between the two mass definitions. In the case of the KiDS-WHL comparison, the slope is always compatible with 1, while we find larger deviations for the KiDS-DESI case. However, we stress that the mean shift in mass resulting from applying the scaling to the cluster samples we use in the subsequent analysis (not just the sub-samples of matched clusters) is equal to 0.06 dex for WHL and 0.02 dex for DESI, with maximum shifts of 0.09 dex and 0.16 dex respectively. Hence, our mass correction is always below the initial mass uncertainty for individual clusters, and on average much smaller.

We can now use Eq. (4) with the associated best-fit parameters to rescale the masses of WHL and DESI in each redshift bin. As DESI is the only catalog that extends at $z > 0.8$, its highest redshift clusters have no matches with KiDS; hence, these cluster masses are not rescaled. The right panels of Figs. 3 to 5 show once more the comparison of the masses for cluster matches, but this time after applying the mass rescaling; again, we overplot to the points the bisector and the mean masses with standard deviations for the $y = -x + \Delta$ bins. As already mentioned, our mass correction is overall small, so these plots resemble the ones shown in the left-hand panels. Still, it is possible to appreciate how the agree-

¹¹ <https://docs.scipy.org/doc/scipy/reference/odr.html>.

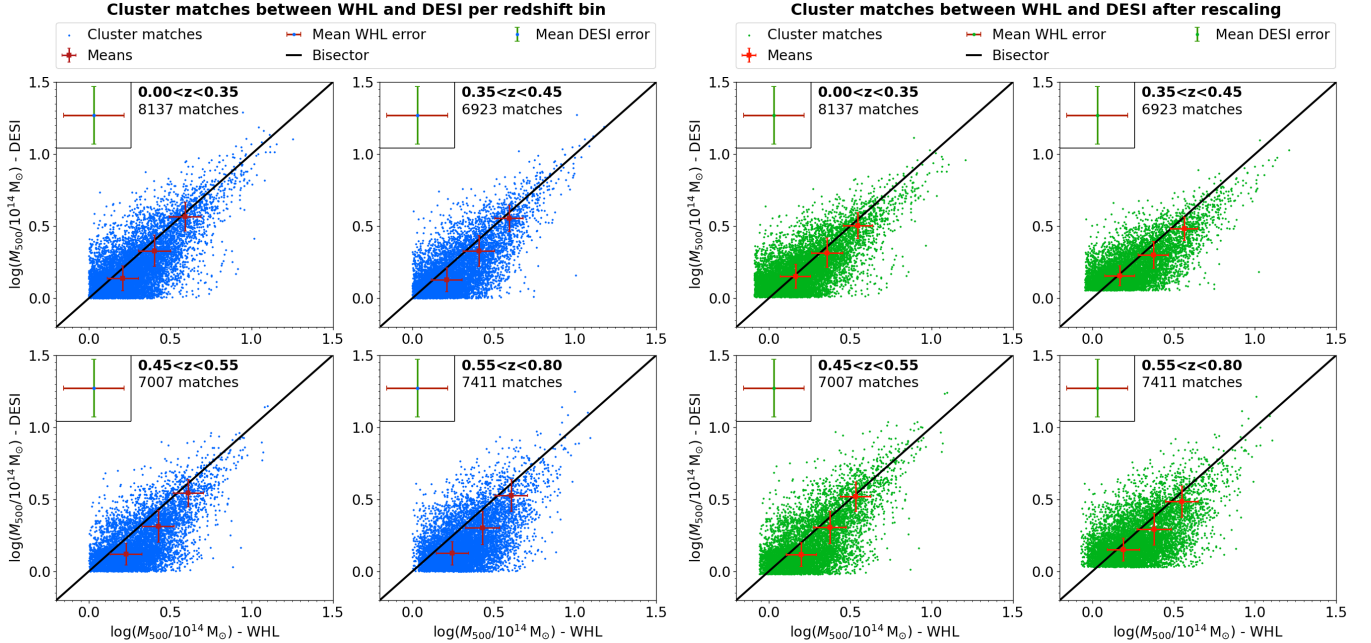


Figure 5. Similar to Fig. 3 and 4, but for the comparison between DESI and WHL. In this case no direct linear regression was employed to scale WHL masses to match DESI values or vice-versa; hence, the left panels do not include any fitting results. The right panels show the comparison between DESI and WHL after being both independently scaled to match the mass values from KiDS. Even in this case, the scaling yields a better agreement between the masses of matched clusters from the two catalogs.

ment between the mean-mass points and the bisector has marginally improved. It is interesting to consider the comparison between WHL and DESI in Fig. 5; we notice that, in this case, no fitting function is overplotted to the plots in the left panel, as we did not consider a direct rescaling of WHL masses to match DESI values, or vice-versa. Instead, both catalogs were re-scaled independently to match KiDS mass values in their associated matches. The comparison between the rescaled WHL and DESI masses is shown in the right panel of Fig. 5. Again, the mean points over the $y = -x + \Delta$ bins show a better agreement with the bisector, thus corroborating the consistency of our approach for mass recalibration.

In Appendix B we quantify what impact this mass rescaling has on the final results of our study. We will repeat the stacking analysis and the parameter estimation on a different version of our cluster sample, obtained by merging the three catalogs without any explicit mass rescaling. We will show that the differences in the final results are indeed much smaller than the statistical uncertainties we quote on our parameter estimates.

3.5. The joint cluster catalog

The mass rescaling described in the previous section is applied to the WHL and DESI catalogs, including also clusters with mass lower than $10^{14} M_{\odot}$; the cut $M_{500} > 10^{14} M_{\odot}$ is then applied subsequently to the

mass-rescaled catalogs. This allows clusters with initial mass below our threshold to be included in the chosen sample if the rescaling increases their M_{500} above $10^{14} M_{\odot}$. All catalogs are then queried to match the footprint of the two ACT patches, which results in 806, 15,330 and 14,477 clusters in KiDS, WHL and DESI respectively. We then remove cluster repetitions; the latter are identified adopting the same positional matching criteria detailed in Section 3.4. From WHL and DESI we remove all clusters that match KiDS positions while keeping the corresponding entries in the KiDS catalog; as the latter has substantially lower statistics compared to WHL and DESI, this choice ensures no KiDS cluster is discarded. For each remaining repetition between WHL and DESI, we keep the entry from one of these catalogs based on a random choice with equal probability. Overall, we remove 3,437 clusters from WHL and 3,356 clusters from DESI.

These cleared catalogs are then merged together to obtain the final sample we employ for our study, which contains 23,820 clusters in total. The sample spans the mass range $M_{500} \in [10^{14.0}, 10^{15.1}] M_{\odot}$ and the redshift range $z \in [0.02, 0.97]$; a summary of the number of clusters for different source catalogs and ACT patches is reported in Table 2. In the end, WHL and DESI contribute with a comparable number of clusters in each ACT patch. The mass and redshift distributions of the

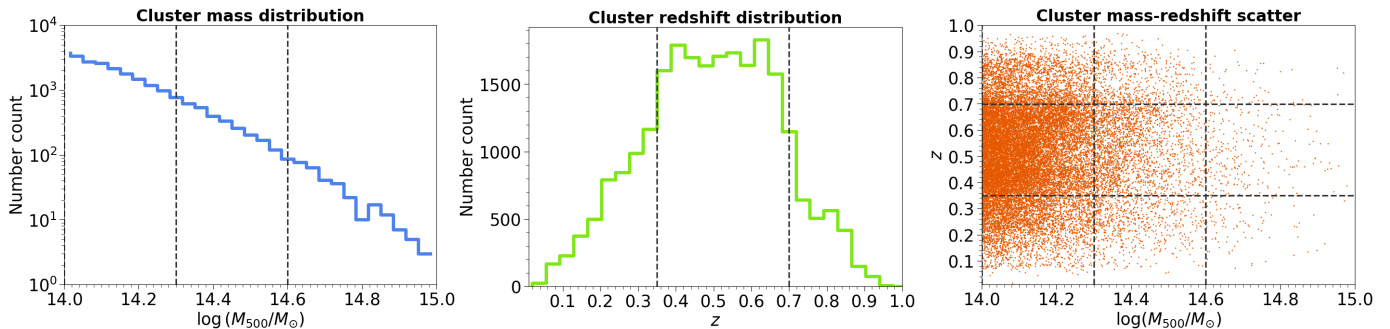


Figure 6. Statistics of the full cluster sample employed in this study. Left and middle panels show the cluster number distributions in mass and redshift, respectively, while the right panel shows the joint distribution of the two variables. In each panel, the dashed lines mark the boundaries of the chosen mass and/or redshift bins, as detailed in Section 4.1.

Table 2. Summary of the contributions from the KiDS, WHL and DESI catalogs to the final cluster sample employed in this analysis. For each catalog we report the number N of clusters overlapping with the ACT footprint, the numbers N_{BN} and N_{D56} of clusters located in the BN and D56 patches respectively, and their redshift spans. These values are referred to the WHL and DESI samples obtained after mass recalibration (Section 3.4) and the removal of overlapping objects (Section 3.5).

Catalog	N	N_{BN}	N_{D56}	$[z_{\text{min}}, z_{\text{max}}]$
KiDS	806	806	0	[0.08, 0.74]
WHL	11893	8937	2956	[0.04, 0.78]
DESI	11121	8735	2386	[0.02, 0.97]
Total	23820	18478	5342	[0.02, 0.97]

final cluster sample, combining objects from both ACT patches, are shown in Fig. 6.

4. THE MEAN CLUSTER COMPTON PROFILES

In this section we describe the methodology we adopt to measure the mean angular y profiles from our cluster samples, and discuss the results.

4.1. Cluster binning

The main goal of this study is to explore the dependence of the cluster pressure profile on mass and redshift. To this aim, we define a set of three bins in $\log_{10}(M_{500})$, bounded by the values [14.0, 14.3, 14.6, 15.1], and three bins in z , bounded by the values [0.00, 0.35, 0.70, 1.00]. We then split our cluster catalog into a set of nine sub-samples, each belonging to the combination of a mass bin and a redshift bin. The last panel in Fig. 6 is a scatter plot showing the distribution of clusters in the $(\log_{10}(M_{500}), z)$ plane; this plot shows that there is no strong correlation between the two variables, most likely as a result of the catalogs being nearly complete above the chosen mass cut, so that the choice of a redshift

bin is independent of the choice of a mass bin and it is meaningful to adopt the same set of M_{500} boundaries across the whole z range. We also consider the marginalized samples obtained by joining all redshift values for each mass bin, and vice-versa. Finally, we include the full cluster sample as the marginalized case over both variables. We obtain this way a total of 16 different cluster samples (the full sample, 9 disjoint sub-samples and 6 marginalized cases), which we employ separately to measure the mean Compton parameter profile. Hereafter, we shall refer to them as M - z bins.

Our choice for the number of bins in M_{500} and z ensures we have enough statistics for the stacking analysis in each M - z bin, while at the same time allowing to investigate possible dependences in mass and redshift. We follow the same choice adopted in G19 and consider three bins in redshift, almost equally spaced over the range spanned by the cluster sample. We also adopt three bins for the mass; however, given the steep decrease in the number of objects for increasing masses, in this case the top M_{500} bin is chosen wider in order to retain sufficient statistics for the stacking analysis described in Section 4.2. Clearly, in the end we still have a different number of clusters in each M - z bin; this, however, is not an issue in our analysis. The formalism we adopt to model our measurements, which is described in Section 5.3, naturally accounts for the number of objects and the mass span of each case. The final number of clusters included in each M - z bin is reported in Table 3.

4.2. Cluster stacks and angular profiles

For each of our 16 cluster samples we obtain an independent stacked map. Let N_{cl} be the number of clusters in one M - z bin; for the generic i -th cluster we trim a local sub-map centered on its nominal coordinates, with size $30' \times 30'$ in the case of *Planck* and $15' \times 15'$ in the

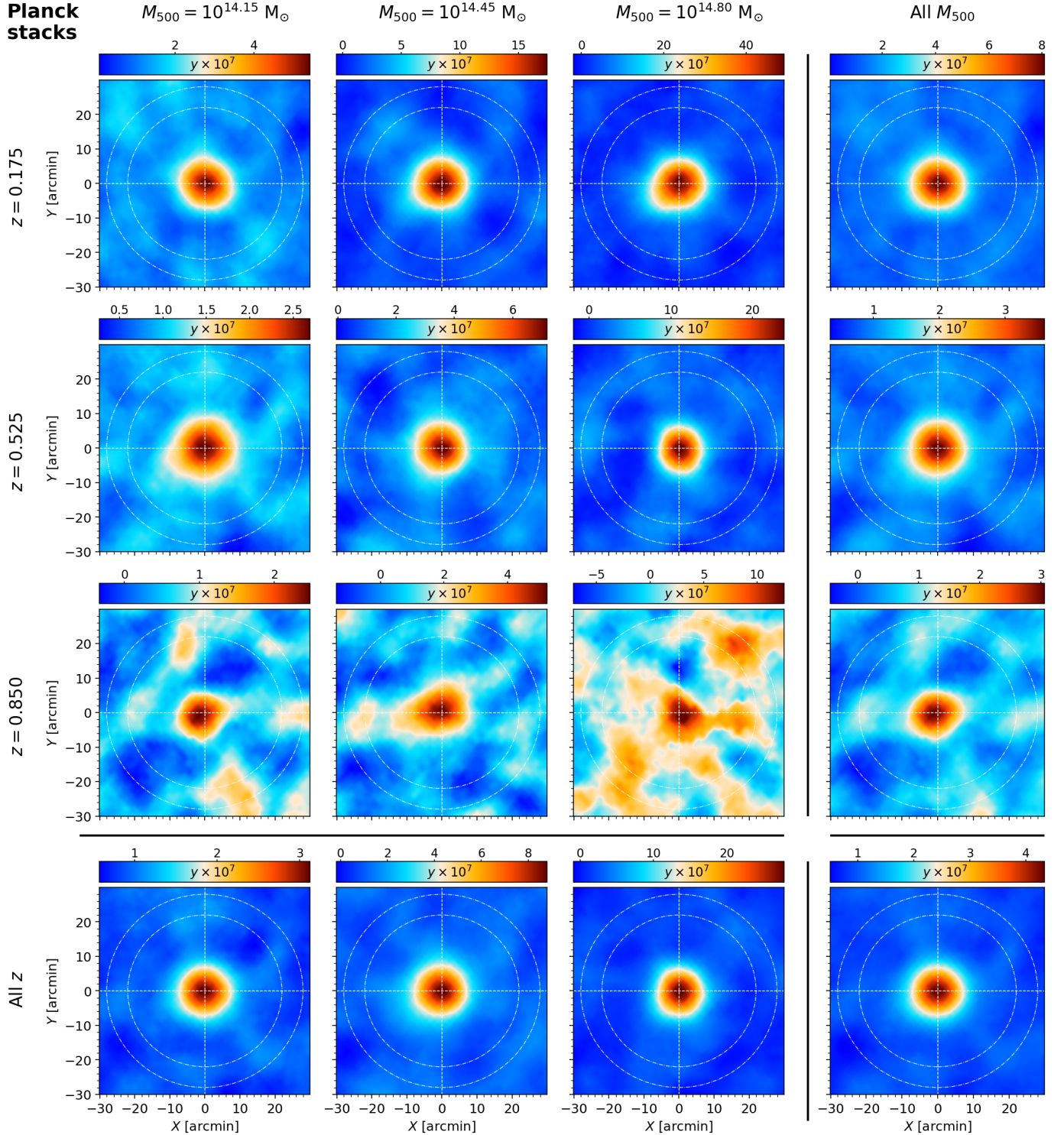


Figure 7. Stacking results for the *Planck* y -map. Each row (column) represents a selected redshift (mass) bin, with the last one showing the marginalized case over the full redshift (mass) range. Notice that the color scale reported above each panel is not the same and is chosen to saturate each stack. In each panel, the nominal center of the stack is marked by dashed white lines, while dot-dashed lines mark the inner and outer boundaries of the annulus employed to estimate the mean background level.

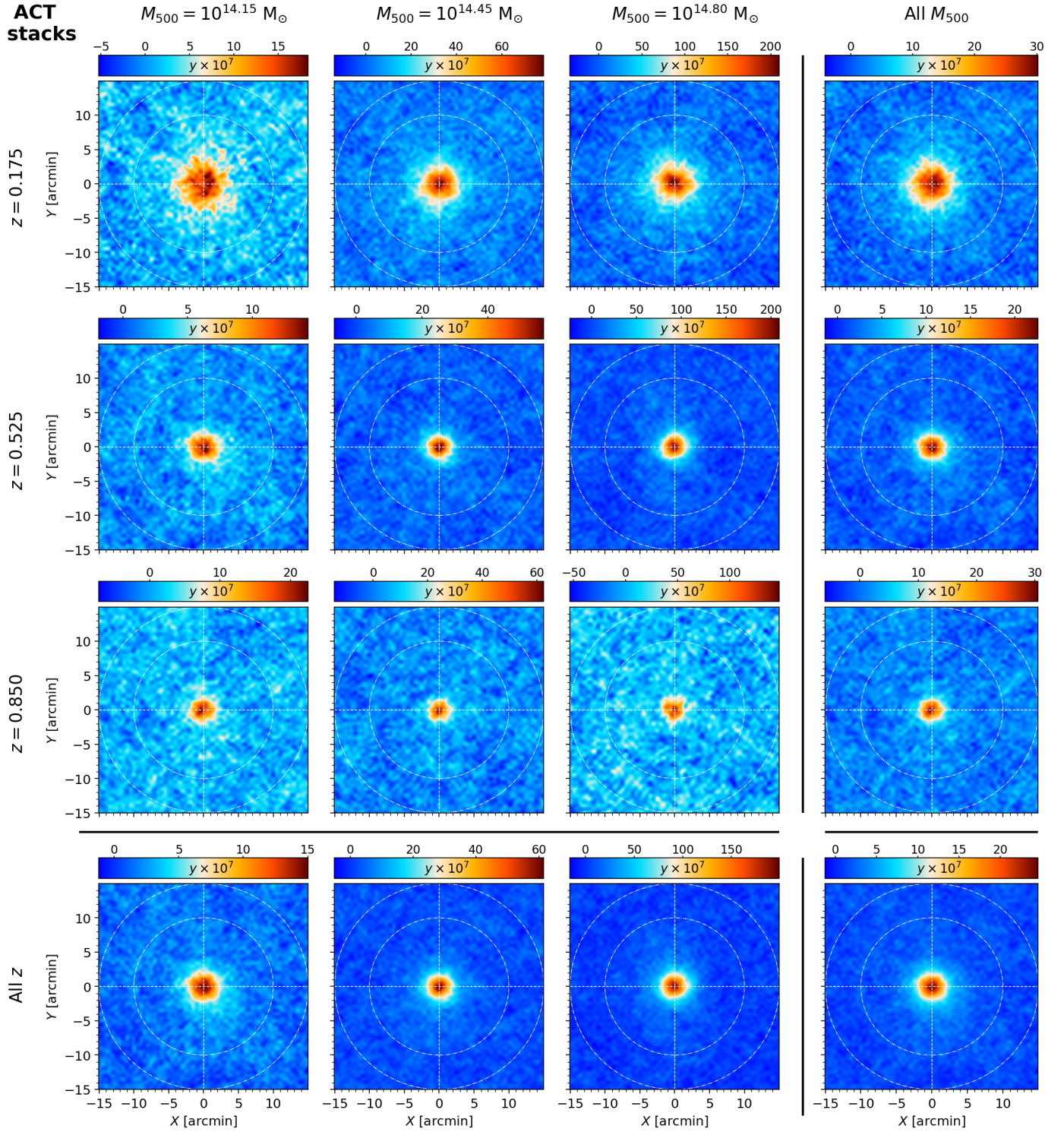


Figure 8. Same as in Fig. 7 but for the ACT y -map.

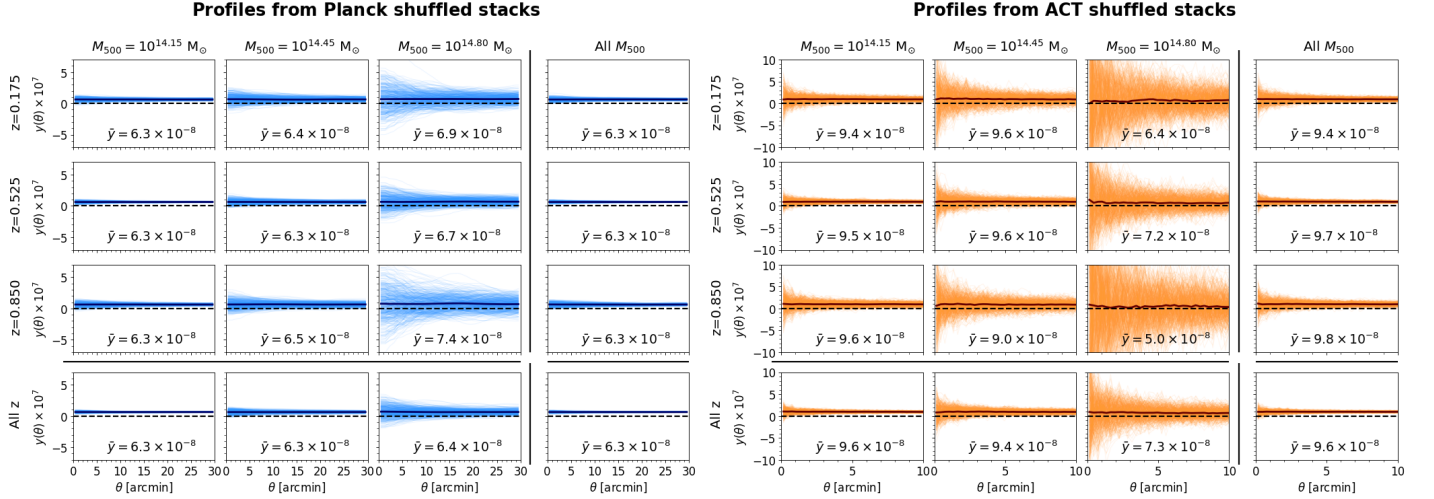


Figure 9. Estimation of the mean background value for each M - z bin for both *Planck* (left) and ACT (right) maps. For each panel we show the profiles obtained by stacking 500 replicas of the corresponding cluster sample, each obtained by randomly shuffling the cluster positions. The thicker solid line shows instead the average profile; the mean amplitude \bar{y} of the latter over the considered angular range is quoted explicitly in each panel. The zero level is marked by a dashed line.

case of ACT¹². We label S_i such a map, which carries the information on the y signal around the cluster; we also obtain an equivalent weight map W_i extracted in the same way from the corresponding survey mask. The y stack map S for the considered sample is then obtained as:

$$S = \frac{1}{W} \sum_{i=1}^{N_{\text{cl}}} S_i W_i, \quad (5)$$

where the total weight is given by:

$$W = \sum_{i=1}^{N_{\text{cl}}} W_i. \quad (6)$$

The resulting 16 stacks for each M - z bin are shown in Fig. 7 for the *Planck* map and in Fig. 8 for the ACT map. For each stack, the axes show the angular separation from the center, which is also marked with a pair of white dashed lines.

From each of these stacks we can derive the associated Compton parameter profile, $y(\theta)$, as a function of the angular separation θ from the cluster center. The profile is built by splitting the pixels over a set of N_b bins in the angular separation from the map center and taking their mean value in each bin. As we are interested in the contrast of the local cluster signal, we first quantify a mean background value to be subtracted from each map¹³. The latter is estimated by repeating, for each

M - z bin, the Compton y stack using 500 different replicas of the associated cluster sample, where in each case the cluster coordinates are randomly shuffled within the allowed ACT footprint. This results in 500 radial profiles per M - z bin; the resulting mean is used to evaluate the background contribution as a function of θ , and is subtracted from the corresponding M - z stack obtained using the real cluster sample. The results are shown in Fig. 9 for both ACT and *Planck*. We notice that in all cases the mean profile does not show any strong dependence on the angular separation from the center; we then quote in each panel the mean value \bar{y} of the average profile over the considered θ range (i.e., up to 30 arcmin for *Planck* and 10 arcmin for ACT). We stress that clusters from different M - z bins actually span the same area, which is set by the ACT patch boundaries. Hence, we would expect to obtain the same estimate for the mean background level using different cluster samples. Fig. 9 shows that this is in general verified, with the exception of the top mass bin which displays larger deviations. This is due to the much lower number of clusters in this mass range, which produces a considerably larger spread of the individual shuffled profiles around the mean (the effect is more relevant for ACT). However, for all these M - z bins the stack amplitude from Fig. 7 and 8 is high enough that this zero-level correction is negligible ($\lesssim 1\%$ at the profile peak). For the lower mass bins, instead, the estimate of the mean background level converges to the values of $\bar{y} = 6.3 \times 10^{-8}$ for *Planck* and $\bar{y} = 9.6 \times 10^{-8}$ for ACT.

Even after the removal of the background contribution as described above, the y profiles do not always reach a null amplitude for large θ values. We then sub-

¹² These different values are a result of the different beam size for the two maps, and they were chosen to enable a reconstruction of the whole cluster signal and part of the neighboring background, see Figs. 7 and 8.

¹³ The stacks plotted in Fig. 7 and 8 are not background-subtracted.

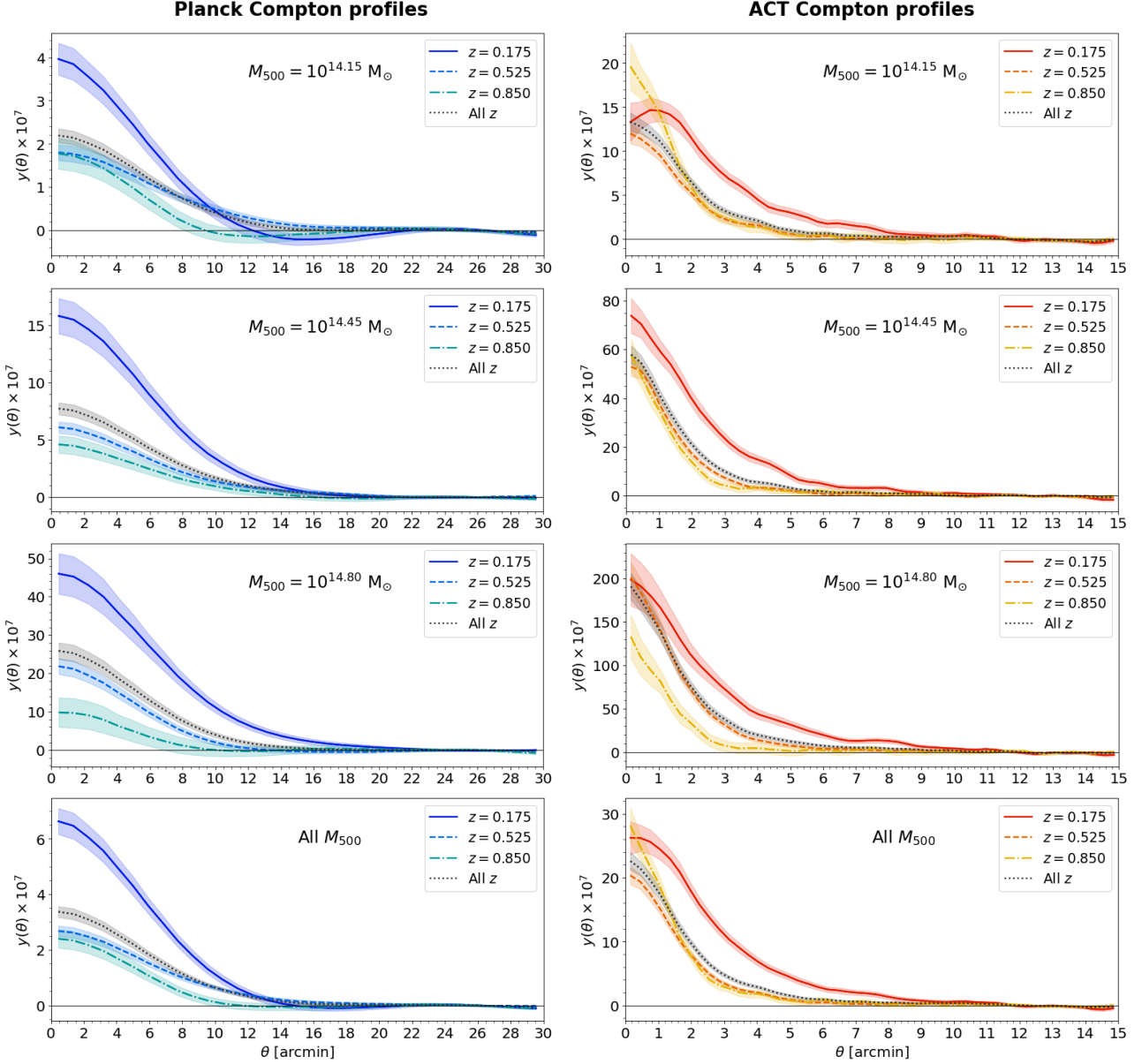


Figure 10. Radial profiles obtained from the stacks shown in Figs. 7 and 8. The left column shows the results for *Planck*, the right column the results for ACT. Each row corresponds to a chosen M_{500} bin, with the bottom row showing the marginalized case over all masses. Each panel shows the results from the three redshift bins and for the marginalized case over all redshifts; the shaded area around each profile quantifies the associated $1-\sigma$ uncertainty.

tract from each profile an additional zero-level contribution measured as the average of the y values from pixels bounded by a circular annulus outside the cluster outskirts. The inner and outer annulus radii are [22, 28] arcmin for *Planck*, and [10, 15] arcmin for ACT, chosen in such a way as to leave out any cluster signal contribution (see again Figs. 7 and 8 for a reference). Notice that this operation will be also applied to our theoretical predictions of the cluster profile, see Eq. (31). The final, background-subtracted profiles are shown in

Fig. 10 for both *Planck* and ACT (left and right panels, respectively). These figures focus on the comparison between the profiles from different redshift samples, for each bin in cluster mass.

To complete the statistical characterization of our measurements, we compute the covariance matrices associated with the profiles. Again, for each M - z bin, we perform the stacks of $N_{\text{rand}} = 500$ replicas of the associated cluster sample obtained via bootstrap resampling (each randomized catalog is obtained by randomly se-

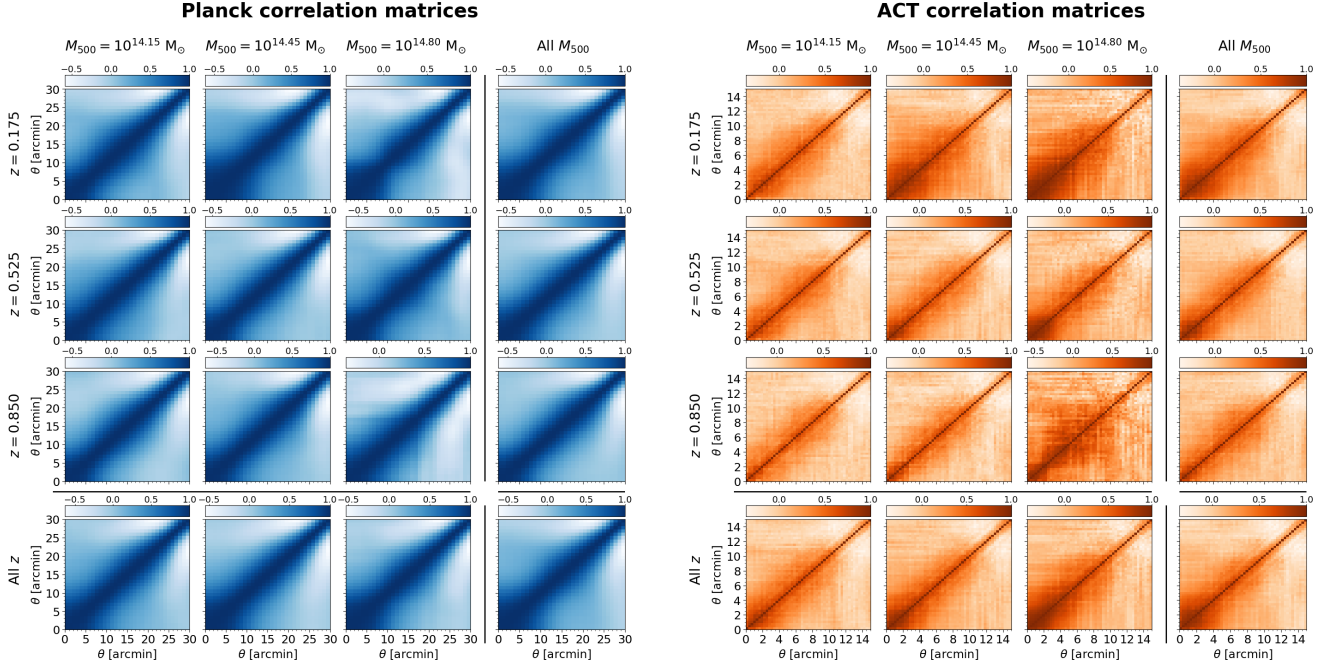


Figure 11. Correlation matrices computed from the randomized stacks as described in Section 4.2. Results are shown for *Planck* on the left and ACT on the right, using the same M_{500}, z binning scheme adopted in Figs. 7 and 8.

lecting clusters from the original sample, up to the same number N_{cl} , with possibility of repetition). The covariance between two angular separations θ_i and θ_j can then be computed as:

$$C(\theta_i, \theta_j) = \frac{1}{N_{\text{rand}}} \times \sum_{k=1}^{N_{\text{rand}}} [y_k(\theta_i) - \bar{y}(\theta_i)] [y_k(\theta_j) - \bar{y}(\theta_j)], \quad (7)$$

where y_k denotes the k -th random profile and \bar{y} is the average profile out of the random realizations:

$$\bar{y}(\theta_i) = \frac{1}{N_{\text{rand}}} \sum_{k=1}^{N_{\text{rand}}} y_k(\theta_i). \quad (8)$$

By construction, the diagonal of each covariance matrix quantifies the profile variance at the corresponding angular separation, $\sigma^2(\theta_i) = C(\theta_i, \theta_i)$; these $\sigma(\theta_i)$ values are the effective uncertainties in our profile measurements, and are shown as shaded regions in Fig. 10. In Fig. 11 we show, for both *Planck* and ACT, the associated 16 correlation matrices, which are obtained from the covariance matrices as:

$$\text{Corr}(\theta_i, \theta_j) = \frac{C(\theta_i, \theta_j)}{\sigma(\theta_i)\sigma(\theta_j)}. \quad (9)$$

The covariance matrices also allow us to compute the significance of the measured y profile for each M - z bin,

defined as the chi-square:

$$\chi^2 = \sum_{i=1}^{N_b} \sum_{j=1}^{N_b} y(\theta_i) I(\theta_i, \theta_j) y(\theta_j), \quad (10)$$

where I is the inverse of the covariance matrix corrected by an overall scaling factor to yield an unbiased estimator (Hartlap et al. 2007):

$$I(\theta_i, \theta_j) = \frac{N_{\text{rand}} - N_b - 2}{N_{\text{rand}} - 1} C^{-1}(\theta_i, \theta_j). \quad (11)$$

The significance for all the stacks is reported in Table 3, together with the number of clusters in each sample. As the quantity from Eq. (10) depends on the number of considered bins, we quote the significance per bin, defined as $\chi_b^2 = \chi^2/N_b$, where N_b is the number of angular bins until the inner radius of the annulus employed to estimate the background value (33 for ACT and 24 for *Planck*). Since we are not using the χ^2 estimate to fit for a model, the number of degrees of freedom is equal to the number of bins. Hence, our χ_b^2 measurement is in fact a reduced- χ^2 measurement for the null model $y(\theta) = 0$, which can be used to evaluate the significance of the detection.

4.3. Discussion of profile measurements

Figs. 7 and 8 show that the cluster signal is clearly detected in all cases; in order to better show its contrast with respect to the background, the color scale is chosen to saturate the signal in each stack. The main difference

Table 3. Significances per bin χ_b^2 on the mean y profile measurements for all the considered M - z bins, for both *Planck* and ACT, computed as in equation (10). The table also reports the number of clusters stacked in each case.

		M_{500}			
		$[10^{14.0}, 10^{14.3}] M_\odot$	$[10^{14.3}, 10^{14.6}] M_\odot$	$[10^{14.6}, 10^{15.1}] M_\odot$	All M_{500}
		z			
N_{cl}		3652	673	96	4421
χ_b^2 (<i>Planck</i>)	[0.00, 0.35]	62.4	107.0	91.4	157.7
χ_b^2 (ACT)		5.8	6.2	5.1	7.8
N_{cl}		13518	2125	243	15886
χ_b^2 (<i>Planck</i>)	[0.35, 0.70]	33.0	76.3	125.5	82.0
χ_b^2 (ACT)		7.6	9.4	6.0	10.0
N_{cl}		2840	620	53	3513
χ_b^2 (<i>Planck</i>)	[0.70, 1.00]	13.3	19.0	23.5	30.1
χ_b^2 (ACT)		4.1	4.3	3.0	6.4
N_{cl}		20010	3418	392	23820
χ_b^2 (<i>Planck</i>)	All z	94.2	160.5	179.6	229.0
χ_b^2 (ACT)		9.7	11.4	7.7	12.4

between *Planck* and ACT results is the resolution of the reconstructed signal, as expected. The much larger *Planck* beam implies not only that the cluster signal is artificially broadened to larger angular separations from the stack center, but also that most of the features on scales below a few arcminutes are smoothed out. The ACT stacks, instead, allow for a more accurate reconstruction of the same signal at smaller scales. A larger beam also implies a more severe dilution of the cluster signal, as it is evident by comparing the amplitude of any stack between the two y maps.

As expected, for each survey we see that the significance of the stacks tends to be lower for decreasing mass and increasing redshift. This is much clearer for the ACT stacks, which are less affected by the smoothing effect of the beam convolution. A reduction in mass determines the highest variations in the signal amplitude and yields in general more irregular stacks. The much higher statistics available for the lowest mass bin (first panel in Fig. 6) ensures the cluster signal is still detected despite the significant drop in the S/N expected for individual objects in this M_{500} range. An increase in redshift also produces a decrease in the signal amplitude (although to a lesser extent compared to the mass change), with the highest redshift bin showing stronger background fluctuations. The small ACT beam also allows us to appreciate the shrinking of the cluster signal for increasing redshift, as the angular diameter distance is monotonically increasing with z in the redshift range we explore. The decrease of the profile amplitude with z could be a result of higher redshift clusters being in

earlier stages of their evolution, and as such possibly not yet fully virialized, which would lower the associated SZ signal (we remind that our cluster sample is selected on the basis of optical observations, which cannot probe directly the ICM). Besides, higher z clusters subtend smaller angular scales and are therefore more severely affected by the beam smoothing effect; this could account for the higher z dependence of the profile amplitude observed in *Planck* stacks compared to ACT stacks. The marginalized cases over M_{500} typically show features in between the ones of the two lowest mass bins, as those encompass the vast majority of clusters in our samples. The marginalized cases over z are instead quite similar to the mid-redshift bin, as the cluster number in different z bins is comparable. Finally, the marginalized case over both M_{500} and z shows the highest S/N and the most regular, rounded cluster emission, as it is expected from the exploitation of the full cluster statistics.

Most of these considerations can also be inferred from the angular profiles in Fig. 10. Notice that, because each panel compares the profiles from different redshift bins, it does not include the associated instrumental beam profile to avoid excessive clutter. A direct comparison between each measured y profile and the beam profile (scaled to the measured peak amplitude) will be shown later in Figs. 13 and 14. Those figures prove that the measured profiles extend to higher angular separations than the instrumental beam, i.e. the profiles are resolved in all cases; it is then meaningful to employ them to fit for the underlying pressure profile parameters (Section 6), even for the case of *Planck*. Going back to

Fig. 10, we see the profiles for *Planck* always show a regular trend, also thanks to the smoothing effect from the large instrumental beam: for a chosen M_{500} bin, the profiles have a similar shape with the amplitude steadily decreasing for increasing z , and with the marginalized case over all redshifts being generally close to the mid- z sample. The higher resolution of ACT allows instead to reveal more irregularities in the profiles. The lowest mass and redshift bin case shows a decrease of the profile amplitude towards the stack center; this results from the peak of the stacked signal being located off-center, as it is also clear from the corresponding stack panel in Fig. 8. This could be due to a possible contamination from neighboring high mass clusters, or to a mismatch between the sample cluster nominal and real central positions; the latter possibility will be taken into account in our modeling in Sec. 5.4. We also notice that for the top mass bin the top and mid redshift bins have a comparable peak amplitude; once again, this is probably due to a miscentering effect, which artificially dilutes the signal amplitude and becomes more relevant for lower redshifts. We conclude this section by commenting on the correlation matrices plotted in Fig. 11. The angular y profile is expected to introduce correlations between neighboring θ bins. This is indeed reflected in the plots, especially for the lowest angular separations. Once again the situation is remarkably different depending on the considered survey, with the correlation extending up to a scale of ~ 1 -2 arcmin in the case of ACT and up to ~ 10 arcmin in the case of *Planck*, as expected from the different FWHMs. For each survey, the correlation matrices do not show an appreciable dependence on the chosen mass and redshift bins. The diagonal values of the covariance matrices are the square of the uncertainties overplotted to the radial profiles as shaded areas in Fig. 10. We see that the number of clusters stacked in each case partially affects the magnitude of the uncertainties, with the marginalized cases generally showing the smaller error bars. This is also reflected in the significance values quoted in Table 3. As expected, the detection significance increases for high masses and low redshifts, for both *Planck* and ACT, but is also partially affected by the number of clusters in the associated sample. We can quote the square root of the χ^2_{ν} values as the detection significances per bin in σ units. The significance per bin is typically above $\sim 3.6\sigma$ for *Planck* and $\sim 1.7\sigma$ for ACT, and reaches the top values 15.1σ and 3.5σ respectively for the stack of the full cluster sample. The higher significances associated with *Planck*'s measurements are a result of the lower uncertainties in the reconstructed profiles, which in turn are due to the smoothing effect of the larger beam.

5. THEORETICAL MODELING

The following details the formalism we adopt to predict theoretically the Compton profiles presented in the previous section.

5.1. The pressure profile for individual clusters

The electron pressure profile P_e for a galaxy cluster of mass M_{500} at redshift z can be written as:

$$P_e(r; M_{500}, z) = P_{500}(M_{500}, z) f(M_{500}, z) \times \mathbb{P}(x = r/\tilde{R}_{500}). \quad (12)$$

Here, $\mathbb{P}(x)$ is the UPP already defined in Eq. (3) and P_{500} is the characteristic cluster pressure expected in the self-similar model:

$$\frac{P_{500}(M_{500}, z)}{\text{keV cm}^{-3}} = 1.65 \times 10^{-3} E(z)^{8/3} \times \left[\frac{(1 - b_h) M_{500}}{3 \times 10^{14} h_{70}^{-1} M_{\odot}} \right]^{2/3} h_{70}^2, \quad (13)$$

where $E(z) \equiv H(z)/H_0 = \sqrt{\Omega_m(1+z)^3 + \Omega_{\Lambda}}$, with $\Omega_{\Lambda} = 1 - \Omega_m$ for flatness, $h_{70} = h/0.7$ and b_h is the hydrostatic mass bias. A similar expression, but without the inclusion of the $(1 - b_h)$ factor, was also employed in Arnaud et al. (2010); in that work cluster masses were derived from scaling relations based on the quantity Y_X , defined as the product between the gas mass within R_{500} and the spectral temperature T_X (see also Nagai et al. 2007). Such mass estimates rely on the assumption of local hydrostatic equilibrium in the ICM, and can therefore be biased with respect to the true cluster masses. As in this paper we employ mass definitions based on lensing observations, which probe the true cluster mass content, we account for this bias by explicitly introducing the $(1 - b_h)$ factor to scale our M_{500} values in Eq. (13). The bias b_h will be let free in our analysis and estimated together with the other UPP parameters. We remind that the introduction of the hydrostatic bias also affects the definition of the scale radius in the computation of the pressure profile, i.e. $x \equiv r/\tilde{R}_{500}$, with $\tilde{R}_{500} = R_{500}(1 - b_h)^{1/3}$.

We notice that Eq. (12) differs from the expression in Eq. (3), which was the initial *ansatz* proposed by Nagai et al. (2007), by an additional factor $f(M_{500}, z)$. The latter determines a break in the self-similarity and was introduced by Arnaud et al. (2010) to accommodate a residual mass dependence found in the scaled X-ray pressure profiles. When parameterized around the same pivot mass $M_{500} = 3 \times 10^{14} h_{70}^{-1} M_{\odot}$, it reads:

$$f(x; M_{500}, z) = \left[\frac{(1 - b_h) M_{500}}{3 \times 10^{14} h_{70}^{-1} M_{\odot}} \right]^{\alpha_p}, \quad (14)$$

with $\alpha_p = 0.12$ and where again we explicitly introduced the bias correction factor $(1 - b_h)$.

5.2. The mean Compton profile for a population of clusters

The profiles obtained from our stacks contain the contribution from a large number of clusters with different mass and redshift values. Formally, such a merged profile can be evaluated as the two-point correlation between the Compton y map and the cluster sample, which in turn can be obtained by inverse Fourier transform of the associated cross-correlation power spectrum C_ℓ^{yc} :

$$y(\theta) = \int d\ell \frac{\ell}{2\pi} J_0(\ell\theta) C_\ell^{yc} B_\ell, \quad (15)$$

with ℓ the multipole and J_0 the zeroth-order Bessel function. In order to account for the instrumental smoothing of the reconstructed Compton map, the expression also includes the beam window function B_ℓ :

$$B_\ell = \exp\left[-\frac{1}{2}\ell(\ell+1)\sigma_b^2\right], \quad (16)$$

where $\sigma_b = \theta_{\text{FWHM}}/\sqrt{8\ln 2}$. The cross-correlation power spectrum C_ℓ^{yc} can be computed using a halo model framework, which considers the contribution of both a one-halo and a two-halo term as (Komatsu & Kitayama 1999):

$$C_\ell^{yc} = C_\ell^{yc,1} + C_\ell^{yc,2}. \quad (17)$$

The one-halo term $C_\ell^{yc,1}$ quantifies the integrated contribution of individual clusters, and is computed as:

$$C_\ell^{yc,1} = \frac{1}{\bar{n}_c} \int dz \frac{d^2V}{d\Omega dz}(z) \int dM \frac{dn}{dM}(M, z) \times S(M, z) \tilde{y}_\ell(M, z), \quad (18)$$

where the integrals are weighted by the comoving volume element $d^2V/d\Omega dz = c\chi^2/H(z)$ (χ is the comoving distance to redshift z) and the halo mass function dn/dM (e.g. Tinker et al. 2008). The selection function $S(M, z)$ depends on the particular cluster sample we consider; it encodes any deviations from the theoretical mass function, due to observational selection effects and other constraints applied to our catalogs. The entire expression is normalized by the mean angular number density of halos \bar{n}_c , given by (see also, e.g., Fang et al. 2012):

$$\bar{n}_c = \int dz \frac{d^2V}{d\Omega dz} \int dM \frac{dn}{dM}(M, z) S(M, z). \quad (19)$$

The quantity \tilde{y}_ℓ in Eq. (18) is the Fourier transform of the Compton parameter profile, which can be computed

as:

$$\tilde{y}_\ell(M, z) = \frac{\sigma_T}{m_e c^2} \frac{4\pi \tilde{R}_{500}}{\ell_s^2} \times \int dx x^2 \frac{\sin(\ell x/\ell_s)}{\ell x/\ell_s} P_e(x; M, z), \quad (20)$$

where $\ell_s = d_A/R_{500}$ and d_A is the angular diameter distance; the expression contains the cluster electron pressure profile P_e defined in Eq. (12) and the radius \tilde{R}_{500} corrected for the hydrostatic bias.

The two-halo term $C_\ell^{yc,2}$ quantifies the correlation between different clusters, and is computed as:

$$C_\ell^{yc,2} = \frac{1}{\bar{n}_c} \int dz \frac{d^2V}{d\Omega dz} W_\ell^y(z) P_m\left(k = \frac{\ell + 0.5}{\chi(z)}, z\right) \times \int dM \frac{dn}{dM}(M, z) S(M, z) b(M, z), \quad (21)$$

where $P_m(k, z)$ is the linear matter power spectrum, $b(M, z)$ is the linear halo bias, and:

$$W_\ell^y(z) = \int dM \frac{dn}{dM}(M, z) b(M, z) \tilde{y}_\ell(M, z). \quad (22)$$

We compute the linear halo bias adopting the parametrization from Tinker et al. (2010).

5.3. Application to our sample

In our case the selection function $S(M, z)$ cannot be simply expressed as a combined cut in mass and redshift, depending on the chosen M - z bin. Due to the extended processing of the cluster catalogs prior to the stacking analysis, as described in Sections 3.4 and 3.5, the selection function cannot be modeled analytically. A solution proposed in G19 consists in splitting the mass and redshift ranges into a set of smaller N_M and N_z intervals¹⁴, respectively. We call \bar{M}_i and \bar{z}_j the mean values within the generic i -th mass and j -th redshift intervals. Within each interval, the integral evaluation can be reasonably approximated as the product of the interval width and the integrand function evaluated at the interval mean value. For the generic i -th mass and j -th redshift interval, the one-halo term then reads:

$$C_\ell^{yc,1}(\bar{M}_i, \bar{z}_j) = \tilde{y}_\ell(\bar{M}_i, \bar{z}_j), \quad (23)$$

i.e., it is simply equal to the Compton Fourier transform evaluated at the mean redshift and mass. For the two-

¹⁴ To avoid confusion we keep using the word ‘‘bin’’ for denoting each of the redshift and mass choices that generate the 16 M - z cluster samples we stacked on the y map, and the word ‘‘interval’’ to designate this further splitting of each bin in smaller separations in mass and redshift.

halo term we have:

$$\mathcal{C}_\ell^{yc,2}(\bar{M}_i, \bar{z}_j) = b(\bar{M}_i, \bar{z}_j) \times P_m \left(k = \frac{\ell + 0.5}{\chi(\bar{z}_j)}, \bar{z}_j \right) W_\ell^y(\bar{z}_j). \quad (24)$$

In this case, the quantity $W_\ell^y(\bar{z}_j)$ still requires to be evaluated via a full mass integral as in Eq. (22). In summary, when working with intervals, Eqs. (23) and (24) replace Eqs. (18) and (21), respectively.

For both the one- and two-halo terms, the full quantity over the chosen cluster sample can be recovered as:

$$\mathcal{C}_\ell^{yc,X} = \frac{1}{N_{\text{cl}}} \sum_i^{N_M} \sum_j^{N_z} n_{ij} \mathcal{C}_\ell^{yc,X}(\bar{M}_i, \bar{z}_j), \quad (25)$$

where X is either 1 or 2, or even the sum of both halo terms. The factor n_{ij} is the number of clusters with mass and redshift within the i -th mass and j -th redshift interval, such that the total number of clusters N_{cl} in the chosen M - z bin is recovered as:

$$N_{\text{cl}} = \sum_{i=1}^{N_M} \sum_{j=1}^{N_z} n_{ij}. \quad (26)$$

The expression in Eq. (25) ensures that, whatever selection is applied to build the considered cluster sample, it will also be accounted for in the theoretical modeling of the associated mean Compton profile.

We stress that a direct approach based on computing the individual $y(\theta; M_{500}, z)$ profile for each stacked cluster and considering the resulting mean value, would not be adequate for our analysis. Firstly, such an approach would not take into account the inter-cluster correlations and only consider the contribution from the one-halo term; secondly, the computation of $\sim 10^4$ profiles would be unpractical for the parameter estimation methodology described in Section 6. The use of Eqs. (23) to (25) allows us to solve both these issues. In our implementation we adopt $N_M = 5$ and $N_z = 5$ when dealing with individual M - z cross-bins, and $N_M = 15$ and $N_z = 15$ when dealing respectively with mass- or redshift-marginalized cases. We checked that this choice yields deviations $< 1\%$ from the theoretical profile obtained adopting the full formalism from Eqs. (18) and (21) (with the n_{ij} factors computed integrating the halo mass function over the chosen mass and redshift intervals), which is within the error bars of our measurements (Fig. 10).

5.4. Miscentering and zero-level

In our modeling we consider possible offsets of the real cluster centers with respect to their quoted coordinates (Yan et al. 2020). For the stacking analysis this

would imply that the reconstructed profile is artificially diluted, so that we actually measure a mean ‘‘offset’’ profile $\bar{y}_{\text{off}}(\theta)$ instead of the true intrinsic profile $y(\theta)$. We follow the approach presented in Bellagamba et al. (2018) and Giocoli et al. (2021), and divide the cluster population into a fraction f_{off} which is affected by miscentering and a fraction $1 - f_{\text{off}}$ whose cluster true positions coincide with the nominal ones. The resulting observed, miscentered profile y_{msc} is then:

$$y_{\text{msc}}(\theta) = f_{\text{off}} \bar{y}_{\text{off}}(\theta) + (1 - f_{\text{off}}) y(\theta). \quad (27)$$

The problem reduces therefore to the computation of the mean offset profile $\bar{y}_{\text{off}}(\theta)$. For a known angular offset θ_{off} , the miscentered profile $y_{\text{off}}(\theta|\theta_{\text{off}})$ can be computed starting from the centered profile $y(\theta)$ as (Yang et al. 2006):

$$y_{\text{off}}(\theta|\theta_{\text{off}}) = \frac{1}{2\pi} \times \int_0^\infty d\varphi y \left(\sqrt{(\theta^2 + \theta_{\text{off}}^2 + 2\theta\theta_{\text{off}} \cos \varphi)} \right), \quad (28)$$

i.e., integrating a set of profiles whose center is located θ_{off} away from the nominal position, over all possible directions.

The value of the miscentering offset θ_{off} is generally not known *a priori*. Previous work found it reasonably follows a Rayleigh distribution with parameter σ_{off} (Johnston et al. 2007):

$$P(\theta_{\text{off}}, \sigma_{\text{off}}) = \frac{\theta_{\text{off}}}{\sigma_{\text{off}}^2} \exp \left[-\frac{1}{2} \left(\frac{\theta_{\text{off}}}{\sigma_{\text{off}}} \right)^2 \right], \quad (29)$$

so that the expected value for the offset is¹⁵ $\theta_{\text{off}} \simeq 1.25 \sigma_{\text{off}}$. The mean miscentered profile $\bar{y}_{\text{off}}(\theta)$ can then be evaluated by averaging over all possible values of the miscentering, weighted by its probability distribution:

$$\bar{y}_{\text{off}}(\theta|\sigma_{\text{off}}) = \int_0^\infty d\theta_{\text{off}} P(\theta_{\text{off}}, \sigma_{\text{off}}) y_{\text{off}}(\theta|\theta_{\text{off}}). \quad (30)$$

In our analysis both the miscentering offset σ_{off} and the fraction of miscentered profiles f_{off} are taken as free parameters.

As a very last step in our theoretical prediction, we subtract from the profile its zero level:

$$y_{\text{theo}}(\theta) = y_{\text{msc}}(\theta) - \bar{y}_{\text{bkg}}. \quad (31)$$

¹⁵ Hereafter we shall refer to the parameter σ_{off} as the miscentering offset, although the real angular displacement is quantified by θ_{off} .

The background value \bar{y}_{bkg} is computed as the mean of the profile amplitude over the same θ range that was considered in Section 4.2 when computing the zero-level for the profiles measured from the y stacks.

6. PARAMETER ESTIMATION

In this section we present the results on the estimates of the pressure profile parameters.

6.1. Methodology

The ultimate goal of this study is to provide novel estimates of the parameters entering the expression of the universal pressure profile in Eq. (3). As our analysis is based on tSZ measurements alone, without the inclusion of numerical simulations or X-ray data, we do not fit for the central slope of the profile, which we fix to the fiducial value $\gamma = 0.31$, as it was done in similar tSZ-based works (Table 1). In addition, we fit for the hydrostatic mass bias b_{h} and for the values of the miscentering offset σ_{off} and fraction f_{off} . Our parameter space is then 7-dimensional, with a generic parameter state Θ defined as the list of values:

$$\Theta = \{P_0, c_{500}, \alpha, \beta, b_{\text{h}}, \sigma_{\text{off}}, f_{\text{off}}\}. \quad (32)$$

For a given set of the aforementioned parameters, the formalism described in Section 5 allows us to compute the associated profile $y(\Theta)$.

For each of the 16 cluster samples, we fit the theoretical prediction $y(\Theta)$ against the profile y^{obs} extracted from the stack. The best-fit parameters are defined as the set Θ_{bf} that maximizes the likelihood:

$$\mathcal{L}(\Theta) = \exp \left[-\frac{1}{2} (y(\Theta) - y^{\text{obs}})^{\text{T}} C^{-1} (y(\Theta) - y^{\text{obs}}) \right], \quad (33)$$

where C is the covariance matrix measured for the chosen sample as described in Section 4.2. In fact, due to the relative high number of parameters, a direct maximization of the likelihood is not feasible; we adopt instead a Markov chain Monte Carlo (MCMC) approach to explore the parameter space. Specifically, we employ the `Python emcee` package, which is an implementation of the affine invariant ensemble sampler from Goodman & Weare (2010). We adopt flat, uninformative priors on all parameters; the associated ranges are quoted in Tables 4 and 5. After burn-in removal and chain thinning, for each mass and redshift bin we are left with ~ 5000 samples of the posterior distribution on each parameter. The resulting joint probability contours for all parameter pairs, and the one-dimensional distributions for individual parameters, are shown in Fig. 12 for both

Planck and ACT. The figure shows the results for the parameter estimation on the full catalog; the posteriors for all the others M - z bins are qualitatively similar, and are shown in Appendix B.

We consider two different approaches to determine the associated parameter estimates. Firstly, we retrieve the 7-tuple of parameters yielding the maximum value for the posterior probability distribution; we shall refer to these values as the MAP (maximum *a posteriori*) estimates. Since we are using flat priors, the maximum of the posterior distribution also corresponds to the maximum of our likelihood from Eq. (33), or in other words, the MAPs are by definition our best-fit values Θ_{bf} . Secondly, we consider estimates computed for each individual parameter as the 50% percentile over its marginalized 1-dimensional posterior distribution (i.e. the distributions plotted along the diagonal of the triangular plots in Fig. 12 and similar); the associated lower and upper error bars are evaluated as the separations from the 16% and 84% percentiles of the distribution, respectively. We shall label the resulting values as the MID (marginalized 1-dimensional) estimates.

In general, the MAP and MID estimates do not necessarily agree. In fact, in situations involving a large number of parameters with non-linear degeneracies, as it is the case with our model, they are expected to show important differences (for an extensive discussion see for example Section 6 in Joachimi et al. 2021). This is clearly visible in Fig. 12, where MAPs are shown as solid green lines and MIDs as dashed black lines. The two sets of parameters carry different information: the MAPs are our best-fit values, and are employed to compute the associated best-fit predictions for the Compton parameter profiles. The comparison with our measurements is shown for all M - z bins in Fig. 13 for *Planck* and in Fig. 14 for ACT. The MIDs, instead, quantify our fiducial 68% confidence level on individual parameters according to their final probability distributions, and can be compared with estimates from other works. The MIDs with associated error bars are quoted in Table 4 for *Planck* and in Table 5 for ACT; they are also plotted in Fig. 15, where it is possible to visualize their dependence on the selected mass and redshift bin.

As already anticipated in Section 3.4, we also conducted an analogous parameter estimation analysis on the y profiles obtained from the merged catalog without any explicit mass rescaling. Hereafter, we shall refer to such profiles as “unscaled”, while we shall refer to the profiles shown in Fig. 10 as “fiducial”. In Figs. 16 and 17 we show, for *Planck* and ACT respectively, a comparison between the fiducial and unscaled profiles, together with the theoretical predictions obtained using

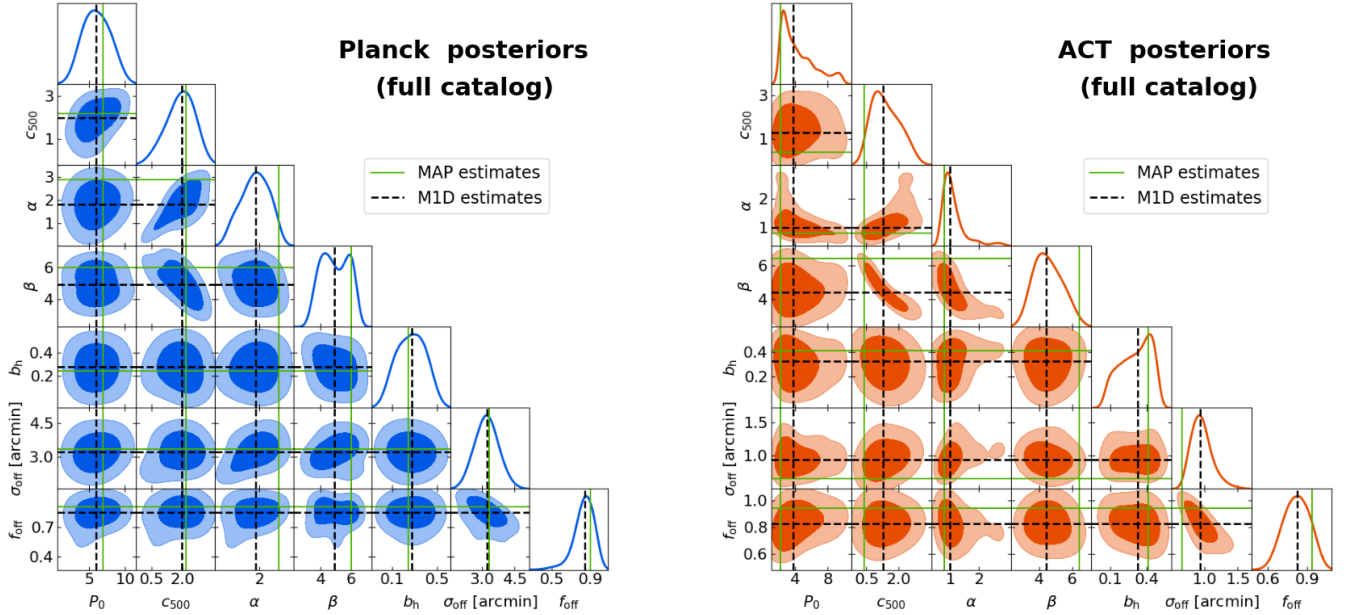


Figure 12. Posterior probability distributions on the model parameters, obtained fitting our theoretical model on the profile corresponding to the stack of the full cluster catalog on *Planck* (left) and ACT (right). Posteriors are plotted as 68% and 95% C.L. contours. The solid green lines mark the best-fit, highest-probability (MAP) values; the dashed black lines mark instead the M1D estimates computed from the marginalized 1-dimensional distributions.

the parameters fitted on the latter. Figs. 18 to 22 show the posterior distributions for both the fiducial and the unscaled profiles. As in these figures the focus is on the comparison between two different sets of contours, we do not mark the locations of the associated MAP and M1D estimates to avoid excessive cluttering.

6.2. Discussion on MCMC results

We begin by commenting the posterior probability contours plotted in Fig. 12 and in Figs. 18 to 22. The main feature of these plots is the asymmetry in the shape of most probability contours. This is a direct result of the complexity of the model we are fitting, and of the strong degeneracy existing between the UPP parameters. Even though the chains are converged (in MCMC terms, the thinned chains are longer than 50 times their autocorrelation length), existing correlations between different parameters produce strong elongations of the contours and yield rather asymmetric posteriors for most of them. Notice that, when fitting this kind of model, this is not an unusual situation, as it can be seen i.e. from Figs. 5 and 7 in G19; especially in the case of ACT, the shape of our posterior distributions on P_0 , c_{500} , α and β mimics the ones presented in that work. In the case of *Planck*, however, the contours are slightly larger and their shape is more regular, which is most likely a result of the smoothing effect induced by the beam and of the resulting extended correlation between neighboring θ bins. The higher resolution of ACT re-

sults instead in tighter contours and overall in a better quality fit.

In this context the difference between the MAP and M1D estimates becomes evident. We verified that the choice of larger priors would yield poorer fitting results for both *Planck* and ACT: for very extended priors, the complex nature of the model leads the chains to encounter local likelihood maxima in positions of the parameter space where the actual values of individual parameters are rather unphysical. As a result, not only would the chains not reach a proper convergence, but also the final posteriors, obtained by the merged contribution of these local maxima, would be artificially broadened and lead to unrealistic M1D estimates. The MAPs, by construction, would still yield best-fit profiles that match the data, but they would not necessarily have a real physical meaning; their combined numerical values would simply be effective in generating a prediction that matches our measurement, but due to the degeneracies in our model, different numerical sets could also provide a good agreement with the data. A physical interpretation of the results requires then our M1D estimates and their posterior distributions. In principle, in order to improve the chain convergence, we could impose Gaussian priors on some of the parameters (e.g., on c_{500} , which typically shows the strongest correlations) based on previous results. We verified that Gaussian priors with the typical uncertainties found in the literature would override the constraining power of the chains

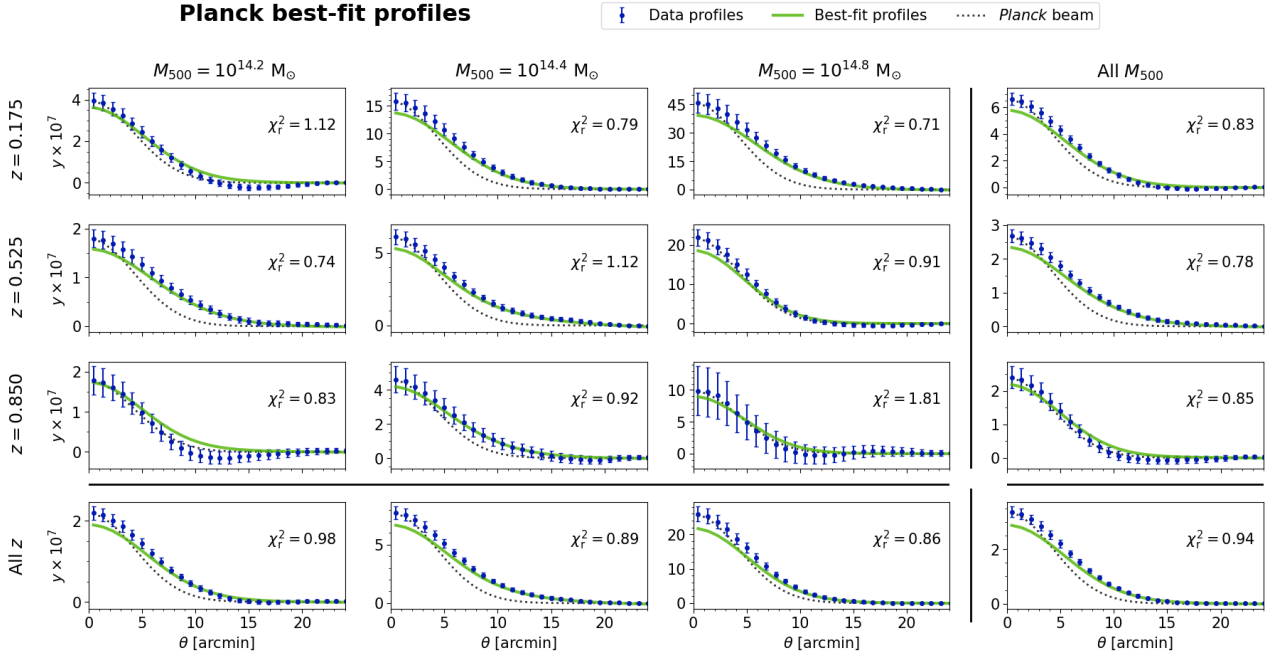


Figure 13. Comparison between the Compton profiles measured on the *Planck* *y* map (data points) and the theoretical profiles (solid line) computed adopting the best-fit (MAP) parameter values, for all the (M_{500}, z) cluster samples considered in this analysis. The plots also show, for reference, the *Planck* beam profile (dashed line) and quote the reduced chi-square values.

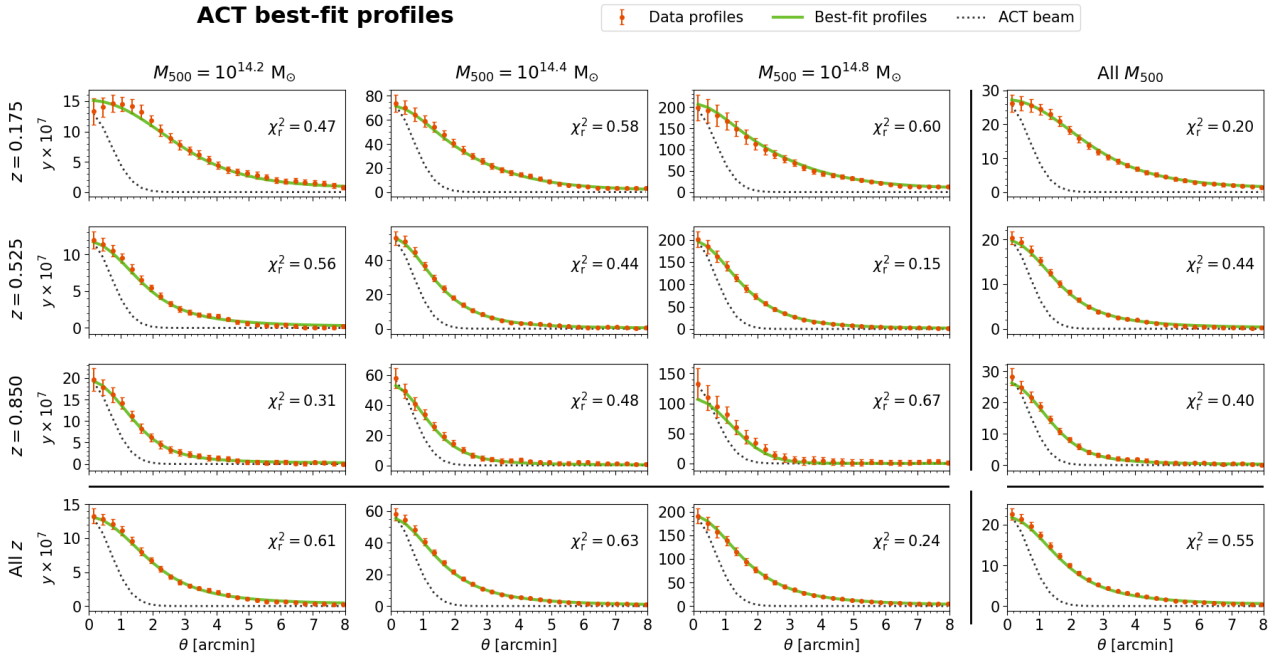


Figure 14. Same as in Fig. 13 but for the ACT profiles.

Table 4. Summary of the M1D parameter estimates for all the considered mass and redshift sub-samples, fitted on *Planck* Compton profiles. Values are computed as the marginalized distribution medians; error bars quantify the 68% C.L.

<i>Planck</i> parameter estimates								
Priors:		[2.0, 10.0]	[0.0, 3.0]	[0.0, 3.0]	[2.0, 6.5]	[0.1, 0.5]	[0.0, 12.0]	[0.0, 1.0]
z	$M_{500}[M_{\odot}]$	P_0	c_{500}	α	β	b_h	$\sigma_{\text{off}}[\text{arcmin}]$	f_{off}
0.175	$10^{14.15}$	$6.4^{+2.2}_{-2.7}$	$2.2^{+0.5}_{-0.6}$	$2.1^{+0.6}_{-0.7}$	$5.1^{+1.0}_{-1.0}$	$0.3^{+0.2}_{-0.1}$	$2.9^{+0.9}_{-0.7}$	$0.7^{+0.2}_{-0.2}$
0.175	$10^{14.45}$	$5.2^{+3.3}_{-2.4}$	$1.7^{+0.7}_{-0.5}$	$1.7^{+0.8}_{-0.6}$	$4.8^{+1.2}_{-0.9}$	$0.2^{+0.2}_{-0.1}$	$3.2^{+0.9}_{-0.7}$	$0.8^{+0.1}_{-0.2}$
0.175	$10^{14.80}$	$5.1^{+3.0}_{-2.1}$	$1.9^{+0.7}_{-0.6}$	$1.9^{+0.7}_{-0.7}$	$4.7^{+1.2}_{-1.1}$	$0.3^{+0.2}_{-0.2}$	$3.4^{+0.8}_{-0.7}$	$0.8^{+0.1}_{-0.1}$
0.175	All M_{500}	$6.2^{+2.6}_{-2.6}$	$2.1^{+0.5}_{-0.5}$	$2.2^{+0.5}_{-0.7}$	$5.3^{+0.8}_{-0.9}$	$0.3^{+0.1}_{-0.1}$	$3.1^{+0.5}_{-0.5}$	$0.9^{+0.1}_{-0.1}$
0.525	$10^{14.15}$	$6.1^{+3.0}_{-2.7}$	$2.2^{+0.5}_{-0.6}$	$1.9^{+0.8}_{-0.9}$	$4.2^{+1.2}_{-0.9}$	$0.3^{+0.1}_{-0.1}$	$4.4^{+1.0}_{-1.0}$	$0.9^{+0.1}_{-0.1}$
0.525	$10^{14.45}$	$4.7^{+3.2}_{-2.0}$	$1.9^{+0.7}_{-0.7}$	$1.1^{+1.5}_{-0.5}$	$3.6^{+0.7}_{-0.4}$	$0.2^{+0.2}_{-0.1}$	$7.2^{+2.9}_{-2.8}$	$0.5^{+0.2}_{-0.4}$
0.525	$10^{14.80}$	$6.4^{+2.0}_{-2.8}$	$1.8^{+0.7}_{-0.7}$	$1.4^{+0.9}_{-0.6}$	$4.9^{+0.9}_{-0.8}$	$0.2^{+0.2}_{-0.1}$	$2.1^{+2.1}_{-1.4}$	$0.3^{+0.3}_{-0.2}$
0.525	All M_{500}	$5.5^{+2.8}_{-2.3}$	$1.9^{+0.7}_{-0.8}$	$1.6^{+0.8}_{-0.7}$	$4.1^{+1.6}_{-0.7}$	$0.3^{+0.1}_{-0.2}$	$4.3^{+0.8}_{-1.2}$	$0.8^{+0.1}_{-0.1}$
0.850	$10^{14.15}$	$5.9^{+2.8}_{-2.4}$	$2.0^{+0.6}_{-0.7}$	$1.8^{+0.9}_{-0.7}$	$4.8^{+1.2}_{-1.0}$	$0.3^{+0.2}_{-0.2}$	$2.9^{+3.5}_{-1.4}$	$0.5^{+0.3}_{-0.3}$
0.850	$10^{14.45}$	$6.0^{+2.9}_{-2.8}$	$2.1^{+0.6}_{-0.7}$	$1.5^{+1.1}_{-0.7}$	$4.2^{+1.3}_{-0.9}$	$0.3^{+0.1}_{-0.1}$	$4.6^{+2.4}_{-2.0}$	$0.6^{+0.2}_{-0.3}$
0.850	$10^{14.80}$	$5.6^{+3.1}_{-2.5}$	$2.2^{+0.5}_{-0.7}$	$1.6^{+0.9}_{-0.7}$	$5.0^{+1.1}_{-0.9}$	$0.3^{+0.1}_{-0.2}$	$4.1^{+5.9}_{-2.7}$	$0.3^{+0.3}_{-0.2}$
0.850	All M_{500}	$6.0^{+2.6}_{-2.3}$	$2.0^{+0.6}_{-0.8}$	$1.6^{+0.9}_{-0.7}$	$5.0^{+0.9}_{-1.1}$	$0.3^{+0.2}_{-0.2}$	$2.6^{+1.5}_{-0.8}$	$0.7^{+0.2}_{-0.3}$
All z	$10^{14.15}$	$5.7^{+2.6}_{-2.3}$	$2.0^{+0.6}_{-0.6}$	$1.9^{+0.8}_{-0.6}$	$5.0^{+0.9}_{-0.9}$	$0.3^{+0.2}_{-0.1}$	$3.3^{+0.5}_{-0.4}$	$0.9^{+0.1}_{-0.1}$
All z	$10^{14.45}$	$6.0^{+2.5}_{-2.2}$	$1.8^{+1.0}_{-1.0}$	$1.4^{+0.9}_{-0.7}$	$4.1^{+1.4}_{-0.9}$	$0.3^{+0.1}_{-0.1}$	$5.0^{+1.9}_{-1.7}$	$0.6^{+0.1}_{-0.2}$
All z	$10^{14.80}$	$6.8^{+2.8}_{-3.6}$	$1.9^{+0.6}_{-0.8}$	$1.6^{+1.0}_{-0.8}$	$5.2^{+0.7}_{-1.0}$	$0.2^{+0.2}_{-0.1}$	$2.3^{+0.6}_{-0.8}$	$0.7^{+0.2}_{-0.3}$
All z	All M_{500}	$5.9^{+2.3}_{-2.0}$	$2.0^{+0.7}_{-0.7}$	$1.8^{+0.7}_{-0.7}$	$4.9^{+1.2}_{-1.0}$	$0.3^{+0.1}_{-0.2}$	$3.2^{+0.5}_{-0.6}$	$0.8^{+0.1}_{-0.1}$

Table 5. Summary of the M1D parameter estimates for all the considered mass and redshift sub-samples, fitted on ACT Compton profiles. Values are computed as the marginalized distribution medians; error bars quantify the 68% C.L.

ACT parameter estimates								
Priors:		[2.0, 10.0]	[0.0, 3.0]	[0.0, 3.0]	[2.0, 6.5]	[0.1, 0.5]	[0.0, 3.0]	[0.0, 1.0]
z	$M_{500}[M_{\odot}]$	P_0	c_{500}	α	β	b_h	$\sigma_{\text{off}}[\text{arcmin}]$	f_{off}
0.175	$10^{14.15}$	$5.1^{+3.0}_{-2.2}$	$2.0^{+0.7}_{-0.7}$	$1.6^{+0.8}_{-0.5}$	$4.2^{+1.0}_{-0.6}$	$0.3^{+0.1}_{-0.2}$	$1.8^{+0.3}_{-0.2}$	$1.0^{+0.0}_{-0.0}$
0.175	$10^{14.45}$	$4.2^{+3.1}_{-1.7}$	$1.9^{+0.6}_{-0.6}$	$1.9^{+0.6}_{-0.6}$	$4.5^{+1.1}_{-0.8}$	$0.3^{+0.1}_{-0.1}$	$1.8^{+0.5}_{-0.4}$	$0.7^{+0.1}_{-0.1}$
0.175	$10^{14.80}$	$5.0^{+3.0}_{-2.2}$	$2.0^{+0.6}_{-0.7}$	$1.5^{+0.7}_{-0.4}$	$4.2^{+1.0}_{-0.7}$	$0.3^{+0.1}_{-0.2}$	$1.7^{+0.5}_{-0.5}$	$0.6^{+0.1}_{-0.2}$
0.175	All M_{500}	$4.3^{+3.1}_{-1.7}$	$1.8^{+0.7}_{-0.6}$	$1.5^{+0.8}_{-0.5}$	$4.2^{+1.0}_{-0.6}$	$0.3^{+0.1}_{-0.2}$	$1.5^{+0.3}_{-0.2}$	$0.9^{+0.1}_{-0.1}$
0.525	$10^{14.15}$	$4.1^{+3.0}_{-1.6}$	$1.6^{+0.8}_{-0.7}$	$1.1^{+0.8}_{-0.4}$	$4.4^{+1.2}_{-0.9}$	$0.3^{+0.1}_{-0.2}$	$1.2^{+0.4}_{-0.3}$	$0.8^{+0.1}_{-0.1}$
0.525	$10^{14.45}$	$4.2^{+3.5}_{-1.7}$	$1.7^{+0.8}_{-0.7}$	$1.5^{+1.0}_{-0.6}$	$4.5^{+1.1}_{-0.8}$	$0.3^{+0.1}_{-0.2}$	$1.2^{+0.4}_{-0.5}$	$0.6^{+0.1}_{-0.1}$
0.525	$10^{14.80}$	$4.0^{+3.0}_{-1.5}$	$1.7^{+0.8}_{-0.6}$	$1.6^{+0.6}_{-0.4}$	$4.5^{+1.1}_{-0.8}$	$0.3^{+0.1}_{-0.2}$	$1.1^{+0.5}_{-0.4}$	$0.5^{+0.2}_{-0.2}$
0.525	All M_{500}	$4.2^{+3.0}_{-1.7}$	$1.3^{+0.9}_{-0.6}$	$1.0^{+0.6}_{-0.2}$	$4.6^{+1.1}_{-0.8}$	$0.3^{+0.1}_{-0.1}$	$1.0^{+0.3}_{-0.3}$	$0.7^{+0.1}_{-0.1}$
0.850	$10^{14.15}$	$5.0^{+3.1}_{-2.1}$	$1.8^{+0.8}_{-0.9}$	$1.3^{+0.8}_{-0.4}$	$4.3^{+1.4}_{-0.9}$	$0.3^{+0.1}_{-0.2}$	$0.9^{+0.5}_{-0.3}$	$0.8^{+0.2}_{-0.2}$
0.850	$10^{14.45}$	$5.4^{+2.9}_{-2.5}$	$2.0^{+0.7}_{-0.9}$	$1.2^{+0.7}_{-0.4}$	$4.2^{+1.0}_{-0.7}$	$0.3^{+0.1}_{-0.2}$	$0.7^{+0.5}_{-0.4}$	$0.5^{+0.3}_{-0.3}$
0.850	$10^{14.80}$	$4.6^{+3.0}_{-2.0}$	$2.3^{+0.5}_{-0.8}$	$1.4^{+0.8}_{-0.5}$	$4.6^{+1.1}_{-1.0}$	$0.3^{+0.1}_{-0.2}$	$0.8^{+1.4}_{-0.3}$	$0.6^{+0.3}_{-0.4}$
0.850	All M_{500}	$5.1^{+3.2}_{-2.5}$	$1.8^{+0.8}_{-0.7}$	$1.2^{+0.7}_{-0.3}$	$4.2^{+1.2}_{-0.7}$	$0.3^{+0.1}_{-0.2}$	$0.8^{+0.3}_{-0.2}$	$0.8^{+0.2}_{-0.2}$
All z	$10^{14.15}$	$4.5^{+2.9}_{-2.0}$	$1.8^{+0.8}_{-1.0}$	$1.1^{+0.6}_{-0.3}$	$4.0^{+1.4}_{-0.5}$	$0.3^{+0.1}_{-0.2}$	$1.1^{+0.2}_{-0.2}$	$0.9^{+0.1}_{-0.1}$
All z	$10^{14.45}$	$3.7^{+3.0}_{-1.3}$	$1.7^{+0.8}_{-0.6}$	$1.3^{+0.7}_{-0.4}$	$4.1^{+0.8}_{-0.5}$	$0.3^{+0.1}_{-0.2}$	$1.2^{+0.5}_{-0.4}$	$0.5^{+0.1}_{-0.1}$
All z	$10^{14.80}$	$3.4^{+4.3}_{-1.1}$	$1.6^{+0.7}_{-0.6}$	$1.4^{+0.6}_{-0.3}$	$4.4^{+1.1}_{-0.7}$	$0.3^{+0.1}_{-0.2}$	$0.9^{+0.4}_{-0.4}$	$0.5^{+0.2}_{-0.2}$
All z	All M_{500}	$3.8^{+2.9}_{-1.4}$	$1.3^{+0.9}_{-0.6}$	$1.0^{+0.4}_{-0.2}$	$4.4^{+1.1}_{-0.8}$	$0.3^{+0.1}_{-0.2}$	$0.9^{+0.2}_{-0.2}$	$0.8^{+0.1}_{-0.1}$

and yield posteriors that resemble the chosen prior distributions. In order to keep our analysis independent from previous works we then maintain flat priors, chosen with a reasonable width in order to encompass other estimates from the literature and at the same time ensure a good convergence of our Markov chains. Clearly, this choice has an effect on the resulting M1D estimates, but it is still less obvious than imposing explicit Gaussian priors.

The plots in Figs. 13 and 14 show that the models computed using our MAP parameters are effective in reproducing the measured profiles across the considered θ range. The figures also report, for each case, the associated reduced chi-square, defined as $\chi_r^2 = \chi^2/N_{\text{dof}}$, where $\chi^2 = -2 \ln \mathcal{L}$ with \mathcal{L} from Eq. (33), and the number of degrees of freedom N_{dof} is computed as the number of angular bins employed in the fit minus the number of free parameters. In the case of ACT we always have $\chi_r^2 < 1$, which proves the good agreement between predictions and data. In the case of *Planck* we generally have higher values and for some bins $\chi_r^2 > 1$; a slight offset of the

prediction with respect to the data is also visible in some of the plots. Once more, this effect has already been observed in the literature (e.g., Fig. 6 in G19). In our case, the offset could be a result of the larger *Planck* beam; the latter, indeed, tends to regularize the bootstrap profiles and reduce their scatter around the mean, thus probably leading to an underestimation of the errors (for the same reason, the significances quoted for our measurements in Table 3 are always higher for *Planck* than for ACT). Besides, a larger beam implies more important correlations between neighbouring angular bins. These two effects result in decreasing the relative importance of the diagonal elements in the covariance matrix compared to the off-diagonal entries (as it can also be appreciated from the correlation plots in Fig. 11). At the parameter estimation level, this can produce the observed offsets in *Planck*'s best-fit profiles.

We turn now our attention to the M1D estimates, and to the effect of mass and redshift on their values. Fig. 15 provides a comprehensive summary, which shows the trend of each parameter when changing M_{500} (differ-

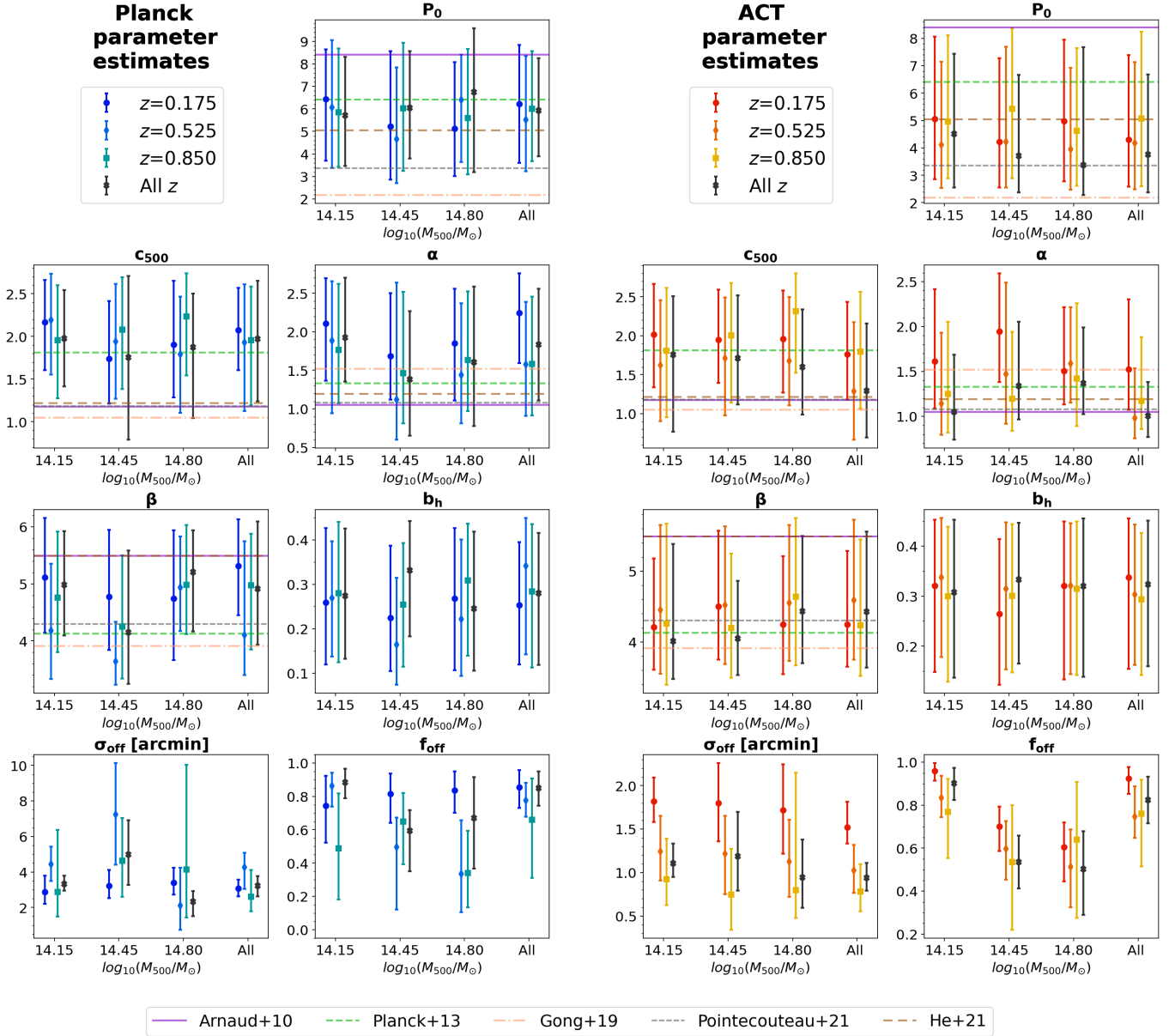


Figure 15. Final estimates on our model parameters, computed as the MID values for the marginalized distributions, obtained from the *Planck* (left) and ACT (right) stacks. Each panel shows the results for an individual parameter, grouping the estimates by mass bin, and showing different redshift bins with different colors and markers as detailed in the plot legend. We also include, in each panel, estimates on the considered parameter obtained by previous works, marked by horizontal solid lines, color-coded as detailed in the bottom of the figure.

ent positions inside each panel) and z (different colors and marker shapes for the points). The most striking feature in these plots is the fact that, regardless of the choice of a mass or redshift bin, all estimates on the UPP parameters are compatible within 1σ . This observation, combined with the good agreement between the best-fit predictions and our measurements, suggests that the universal pressure profile is indeed successful in modeling the ICM electron pressure over the mass and

redshift ranges spanned by our cluster sample. Still, Fig. 15 shows that there are indeed mild variations for the parameters when changing M_{500} or z . Such variations, however, lack in general a consistent trend, so they are no evidence of an effective mass or redshift residual dependence on the UPP parameters. Most likely, this is again a result of the model degeneracy, which also produces the rather large error bars on our estimates. Another feature corroborating this hypothesis is the fact

that the marginalized cluster samples have often values that are not in between the ones obtained from individual bins. We then conclude that the observed variations in the estimates for different M - z bins are just a result of our parameter estimation, and not the evidence of a real residual dependence of the UPP parameters on mass or redshift. We also find a substantial agreement (within the error bars) between *Planck*-based and ACT-based estimates of the UPP parameters.

6.3. Discussion on best-fit estimates

We can now compare our findings with the values obtained from previous studies. Fig. 15 overplots to each panel a few horizontal stripes to mark the location of the results obtained from some of the works listed in Table 1. We observe that our estimates are in general compatible with these previous results. The only exception is the slope at intermediate radii α , for which in the case of *Planck* we obtain somewhat larger values. We stress however that in G19 some of the considered redshift bins yielded even larger values for α , up to 6 in the most extreme case. This large scatter of the estimates obtained from different studies is again the result of the existing degeneracies between the UPP parameters. We conclude that our estimates confirm the results from previous works; the size of our error bars is also comparable with the uncertainties quoted in the literature (when available; see again Table 1).

We comment that studies based on hydrodynamical simulations have also provided insights into possible mass and redshift evolutions of the UPP parameters. The work presented in Battaglia et al. (2012) suggested that P_0 , c_{500} and β require an explicit mass and redshift dependence in order to fit their simulation results (see Table 1 in the reference for details); the analysis in Le Brun et al. (2015) also confirmed the mass dependence of P_0 and c_{500} , finding both parameters increase with M_{500} (Table 2 in the reference). The mass range explored in these works encompasses the one we probe with our cluster sample. We stress, however, that the mass and redshift dependences detected in those studies are in all cases very mild, and can be measured only with the high resolution provided by numerical simulations. In fact, the works in Battaglia et al. (2012) and Le Brun et al. (2015) probe the cluster pressure profile down to radial separations of $r \sim 0.04 R_{200}$ (Figs. 1 and 2 in the reference) and $r \sim 0.1 R_{500}$ (Fig. 3 in the reference), respectively; for our lowest-redshift and highest-mass clusters these values translate into angular scales of the order of ~ 1 arcmin, which even for ACT are comparable with the beam, and where we typically have the largest uncertainties in our profile measurements. Hence, those

mass and redshift variations in the UPP parameters are definitely subdominant in the context of reconstructing the pressure profile from real data, due to a series of factors such as the instrumental beam, residuals in the y map, systematics in the cluster mass estimates and miscentering effects. As far as our measurements are concerned, if an effective dependence of the UPP parameters on M_{500} and z does exist, it is well below the uncertainties in our final estimates.

We move on now to comment our results on the hydrostatic mass bias b_h . Our estimates are typically in the range from 0.2 to 0.3, with somewhat larger values obtained with ACT; the confidence intervals are in any case quite broad, with typical error bars up to ~ 0.2 , and no evident strong degeneracies with the other parameters. A number of different estimates for b_h have been provided in the literature; for a summary, see e.g. table 3 in Ibitoye et al. (2022). Our results are again in agreement with previous findings. Numerical simulation results tend to agree in that the hydrostatic bias has a mass dependence, and can accommodate values for b_h as large as 0.3 for massive clusters (Pearce et al. 2020; Barnes et al. 2021). Our findings are also in agreement with cross-correlation analyses (Makiya et al. 2020; Rotti et al. 2021; Ibitoye et al. 2022) and studies of variously selected cluster samples (von der Linden et al. 2014; Hoekstra et al. 2015; Sereno et al. 2017; Ferragamo et al. 2021; Aguado-Barahona et al. 2022). We stress, however, that our MCMC analysis does not provide strong constraints on the hydrostatic bias.

Finally, the miscentering parameters are the ones that show the largest scatter across different M - z bins. In this case a comparison between *Planck* and ACT is not meaningful, as we set different priors on σ_{off} to account for the considerably different beam size. We find values for σ_{off} around 4 arcmin in the case of *Planck* and around 1.5 arcmin in the case of ACT; for the latter, the miscentering offset is then comparable with the beam FWHM, and is therefore a relatively more important effect, as expected. As for the miscentering fraction f_{off} , we find that in general more than 50% of the clusters in each sample are offset from their nominal position; a mild anti-correlation can be observed between σ_{off} and f_{off} in Fig. 12, which is easily understandable as these parameters produce opposite effects in quantifying the mean miscentering. We also notice from Fig. 15 that this time it is possible to recognize a trend in the M1D values, especially for ACT, with lower redshifts and lower masses requiring a higher miscentering offset. This could have been anticipated by looking at the stacks plotted in Fig. 8, where the lowest masses and redshifts tend to have broader and more irregular profiles. These results

confirm that the miscentering is a necessary inclusion in our theoretical modeling, without which the final estimates on the other UPP parameters would most likely be biased. For example we tested that, without including the miscentering in our theoretical prediction, the resulting estimates on the parameter P_0 are typically very low and unphysical ($P_0 \lesssim 2$); this can be understood as P_0 is the parameter that most directly controls the amplitude of the measured signal, and as such most readily absorbs any dilution effect produced by the miscentering on the profiles.

Before closing this section, we comment on the effect that the mass rescaling we applied to WHL and DESI clusters has on our parameter estimates. Figs. 18 to 22 show the comparison between the final contours obtained from our fiducial profiles and from the unscaled profiles, for all M - z bins and for both *Planck* and ACT. The resulting best-fit predictions for the unscaled profiles (computed based on the associated MAP estimates) are overplotted to the profiles themselves in Figs. 16 and 17. Regarding the agreement between predictions and measurements for the unscaled profiles, similar considerations as for the case of the fiducial profiles apply. As for the final MID parameter constraints, it is clear from the contour plots that the posteriors for the unscaled profiles are almost indistinguishable from the posteriors obtained for the fiducial profiles. Even for the case of the lowest redshift bin, where the two sets of profiles show the largest tensions, the final parameter estimates are rather compatible. This shows once more that the final contour sizes are largely determined by our prior choice and by the correlation between the parameters entering our model; such correlations also result in large error bars and make the estimates overall in agreement. Clearly, the actual, final MID values are not exactly the same, and one could quote the difference between them as a systematic error component to be included in our final parameter uncertainties. In our case, however, such systematic contribution will be much smaller than the statistical uncertainties quoted in Tables 4 and 5. We then conclude that the mass rescaling presented in Section 3.4 has a negligible impact on the final conclusions of this study.

7. CONCLUSIONS

The cluster pressure profile is one of the primary tools to explore the physical state of the ICM; as it is clear from Eq. (2), the Compton parameter y is a very direct probe of the ICM electron pressure, and it has been exploited in this sense by several works in the past decade. In this paper, we explored possible mass and redshift dependences of the parameters governing the shape of the

universal pressure profile in galaxy clusters, by analyzing the y profiles obtained from cluster stacks on Compton parameter maps.

We employed the y -maps delivered by both the *Planck* satellite and the Atacama Cosmology Telescope, the latter limiting the analysis to an effective sky area of $\sim 2,000 \text{ deg}^2$ but at the same time providing a considerably higher angular resolution in the reconstructed tSZ signal. We built a large cluster sample by merging existing galaxy cluster catalogs based on observations from KiDS, SDSS (WHL) and DESI. As cluster masses from these catalogs were estimated following different methodologies, we first homogenized the mass definition by scaling the WHL and DESI cluster masses to the KiDS definition, which is based on weak lensing measurements and is as such less affected by *ad hoc* assumptions on the ICM physical state. The scaling parameters were obtained by comparing the masses from common clusters across pairs of catalogs, for different redshift intervals. After applying a lower mass cut of $10^{14} M_\odot$ (below which we found the stacks would become too noisy) and removing repeated clusters, we merged the three catalogs obtaining a final sample of 23,820 clusters overlapping with the ACT map footprint.

We split these clusters into three mass and three redshift bins, also considering the respective marginalized cases for a total of 16 different cluster samples. We stacked these samples on both the *Planck* and the ACT maps, in all cases obtaining a clear detection of the cluster signal against the background. We extracted a circularly symmetric radial angular profile from each stack map, and computed the associated covariance matrix by repeating the stacks with a set of 500 replicas of the catalog obtained via bootstrap resampling. The covariance matrices allowed us to determine the uncertainties to be assigned to the angular profiles and to compute the significance per bin in their measurements, which is always larger than 13 for *Planck* and 3 for ACT.

We modeled theoretically the mean y profile with a halo-model approach, taking into account the effective cluster mass and redshift distributions in each sample. The theoretical predictions depend not only on the UPP parameters, but also on the hydrostatic bias on the cluster mass, and on two parameters quantifying the magnitude and occurrence of possible miscentering of the clusters from their nominal positions. We then employed the MCMC method to reconstruct the posterior distributions on these parameters with initial flat priors, where the likelihood compares the theoretical prediction with the observed profile using the covariance matrix measured for each cluster sample. In all cases we fixed the pressure profile central slope to $\gamma = 0.31$, as it is custom-

ary in other works based on tSZ data alone. From the MCMC runs we extracted two sets of parameters, the MAPs from the full 7-dimensional likelihood, and the M1Ds from the marginalized 1-dimensional posteriors.

The profile predictions computed with the MAPs provide indeed a good fit to our measurements, yielding $\chi_r^2 < 1$ for almost all cases. The M1D estimates show good agreement between *Planck* and ACT, and with constraints obtained by previous works. The results also do not show any compelling evidence for a residual dependence of the UPP parameters with either M_{500} or z . Although marginal differences are visible, there is no clear trend and the values are largely compatible within the recovered error bars. The main conclusion from this work is that the adopted UPP functional form is effective in describing the ICM electron pressure profile for clusters in the mass range ($10^{14.0} M_\odot < M_{500} < 10^{15.1} M_\odot$) and in the redshift range ($0.02 < z < 0.97$) explored with our clusters. This is the first time the UPP is tested over such a large cluster sample, which is mostly complete within the chosen M_{500} and z limits. We also obtain loose constraints on the hydrostatic mass bias in agreement with previous works based on both numerical simulations and analyses of cluster samples. We prove that miscentering is an important piece of the cluster profile modeling, with more than 50% of the clusters being offset from their nominal position by an amount commensurate with the FWHM value of the corresponding y map. Finally, we showed that possible systematic errors induced by our explicit mass rescaling are well below the statistical uncertainties obtained for each parameter from the MCMC analysis.

ACKNOWLEDGEMENTS

We would like to thank Yan Gong, Zhong-Lue Wen, Joachim Harnois Deraps and Xiaohu Yang for their useful discussions. Based on data products from observa-

tions made with ESO Telescopes at the La Silla Paranal Observatory under programme IDs 177.A-3016, 177.A-3017 and 177.A-3018, and on data products produced by Target/OmegaCEN, INAF-OACN, INAF-OAPD and the KiDS production team, on behalf of the KiDS consortium. OmegaCEN and the KiDS production team acknowledge support by NOVA and NWO-M grants. Members of INAF-OAPD and INAF-OACN also acknowledge the support from the Department of Physics & Astronomy of the University of Padova, and of the Department of Physics of Univ. Federico II (Naples). DT acknowledges the support from the Chinese Academy of Sciences (CAS) President’s International Fellowship Initiative (PIFI) with Grant N. 2020PM0042, and from the National Natural Science Foundation of China (NSFC) Research Fund for International Scientists (RFIS) with Grant N. 12150410315. YZM acknowledges the support of National Research Foundation with grant no. 120385 and 120378, and SARAO group grant. Project 12047503 is supported by National Natural Science Foundation of China. This work was part of the research programme “New Insights into Astrophysics and Cosmology with Theoretical Models confronting Observational Data” of the National Institute for Theoretical and Computational Sciences of South Africa. ZY acknowledges support from the Max Planck Society and the Alexander von Humboldt Foundation in the framework of the Max Planck-Humboldt Research Award endowed by the Federal Ministry of Education and Research (Germany). CG and LM acknowledge the support from the grant PRIN-MIUR 2017 WSCC32 ZOOMING, and the support from the grant ASI n.2018-23-HH.0. CG acknowledges funding from the Italian National Institute of Astrophysics under the grant “Bando PrIN 2019”, PI: Viola Allevato. AHW is supported by an European Research Council Consolidator Grant (No. 770935). MS acknowledges financial contributions from contract ASI-INAF n.2017-14-H.0 and contract INAF mainstream project 1.05.01.86.10.

APPENDIX

A. SUMMARY OF PREVIOUS WORKS

We provide here further information about previous results for the UPP parameters, as an integration of the discussion presented in Section 1. We focus in particular on the cluster-based studies which are listed in Table 1.

The work in [Arnaud et al. \(2010\)](#) considered 33 clusters with $M_{500} \in [1, 10] \times 10^{14} M_\odot$ at $z < 0.2$ observed with *XMM-Newton*, and compared their individual pressure profiles, each scaled by the characteristic

pressure P_{500} ; these clusters were selected from the REFLEX Cluster Survey imposing a lower X-ray luminosity threshold of $0.4 \times 10^{44} h^{-2} \text{ ergs}^{-1}$ in the 0.1 – 2.4 keV band (the REXCESS sample, [Böhringer et al. 2007](#)). REXCESS is by construction a representative sample of an X-ray flux-limited cluster population, which does not privilege specific morphologies or dynamical states in its member clusters. Although finding deviations in the central region between cool-core and morphologically disturbed systems, the scaled profiles in [Arnaud](#)

et al. (2010) showed a good agreement at larger radii, up to R_{500} . The UPP parameters were fitted on the combination of the mean X-ray data profile with the mean profile obtained from numerical simulations, the latter allowing to extend the profile reconstruction beyond R_{500} . This work has been traditionally taken as a reference in all subsequent studies of cluster pressure profiles.

A similar analysis was conducted in Planck Collaboration et al. (2013) on a set of 62 tSZ-detected clusters with $M_{500} \in [2, 20] \times 10^{14} M_{\odot}$ at $z < 0.45$; this cluster sample had already been used to calibrate the tSZ-mass scaling relation in Planck Collaboration et al. (2011b), where it was selected from the *Planck* early SZ source catalog (ESZ, Planck Collaboration et al. 2011a) on the basis of existing high quality *XMM-Newton* observations. This time, information on the pressure profile was obtained from the reconstructed cluster Compton profile, which allowed the authors to explore the ICM gas out to $\sim 3 R_{500}$; the average, derived pressure profile was combined with the average profile obtained from X-ray data. The inclusion of X-ray data allowed to reconstruct the pressure profile down to $0.02 R_{500}$, yielding substantial agreement with SZ data in the overlap range. Again, marginal differences were observed between cool-core and non cool-core clusters, but within the statistical error bars. Compared with results from numerical simulations, the profile in the cluster outskirts was found to be rather flatter, while providing a good agreement at low radii with simulations that implement AGN feedback.

The work in Sayers et al. (2016) considered a set of 47 clusters with $M_{500} \in [3, 25] \times 10^{14} M_{\odot}$ at $z < 0.9$, chosen from observations with *Chandra* and Bolocam (Sayers et al. 2011) on the basis of their redshift and high X-ray temperature; this sample slightly extended the one already studied in Czakon et al. (2015) with the inclusion of two additional clusters. This work focused on the reconstruction of the pressure profile in the cluster outskirts, based on measurements of the integrated y profile from Bolocam and *Planck* data. More precisely, it kept all UPP parameters fixed to the Arnaud et al. (2010) estimates with the exception of the normalization P_0 and the profile slope β at large radii. The best-fit values were found in agreement with results from numerical simulations over the same mass and redshift span of the considered cluster sample. The authors also found evidence for a residual mild dependence of the profile slope on the cluster mass, with more massive clusters favoring higher values of β . Finally, the work acknowledged how these results can be affected by systematics such as sample selection and calibration of cluster masses.

In Pointecouteau et al. (2021) the cluster sample consisted of 31 clusters with $M_{500} \in [3.4, 13.1] \times 10^{14} M_{\odot}$ at $z < 0.71$, which had been previously listed as SZ sources in both *Planck*- and ACT-based catalogs. A major novelty of this work is that the SZ signal was measured on a joint *Planck*-ACT Compton parameter map, built from the linear combination of individual frequency maps from the two surveys as described in Aghanim et al. (2019). The authors extracted y profiles (and derived the associated pressure profiles) for individual clusters in the sample and fitted the resulting mean pressure profile with a UPP model. As the fitting results were strongly affected by parameter degeneracies, the authors fixed both γ and c_{500} to the values from Arnaud et al. (2010). Estimates for the remaining UPP parameters showed broad agreement with previous findings, particularly when it comes to the profile amplitude at the outer radii, while a somewhat larger tension was found at the intermediate radii; the authors mentioned the higher relevance of ACT data (a novelty in this analysis) in this radial range as a possible explanation, while stressing again the limitations inherent to the use of a relatively small, non-representative sample.

Finally, He et al. (2021) employed the same cluster sample (REXCESS) as in Arnaud et al. (2010) and focused on assessing the effect on scaling relations and UPP parameter estimates deriving from the bias between the true cluster mass and the hydrostatic cluster mass sampled by X-ray and SZ observations (see also Section 5.1), an issue that was already acknowledged in Arnaud et al. (2010). The authors fitted the scaling between the two mass definitions on hydrodynamic simulations and employed it to correct cluster masses in the REXCESS sample, finding the initial hydrostatic mass values were underestimated by 7% on average, the effect being larger for higher masses. The scaling was then quantified via a hydrostatic mass bias and incorporated in the formalism by scaling the UPP normalization pressure P_0 and concentration c_{500} (this is equivalent to our treatment of the bias described in Section 5.1, with the difference that we kept the UPP functional form unchanged and scaled the values of M_{500} and R_{500} instead). The authors fitted this modified UPP model on the new mean pressure profile, finding the resulting prediction to yield a reduction in the deviation (quantified by the term in Eq. (14)) from the self-similar model, compared to the original UPP profile.

The list of studies described in this section, and also the summary reported in Table 1, are by no means exhaustive; as the present paper is not intended to be a review on the subject, we redirect to the additional references cited in those works for further reading. We

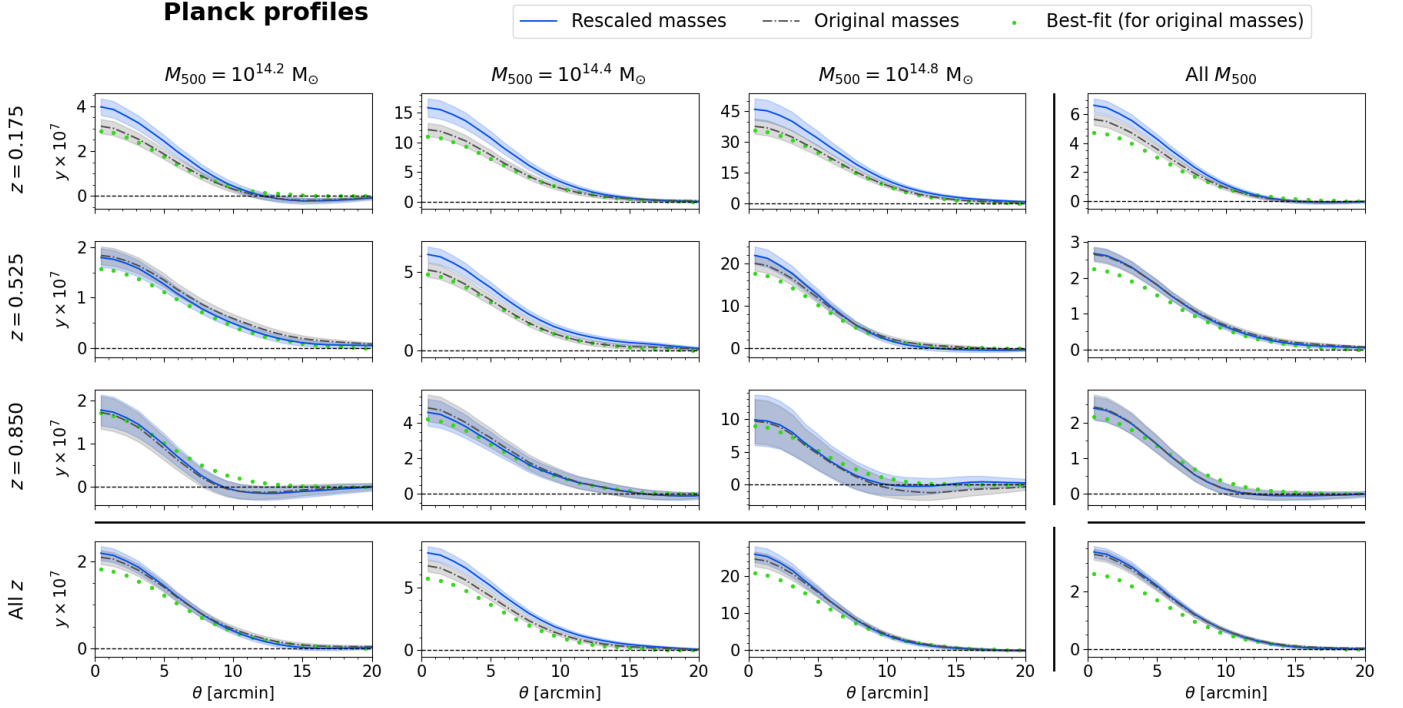


Figure 16. Comparison between the angular y profiles measured on the *Planck* map with the fiducial sample (blue) and the unscaled sample (gray). For both cases the shaded areas quantify the associated uncertainties. We also show with green dots the model predictions for the unscaled profiles, computed using the MAP estimates from the associated MCMC runs.

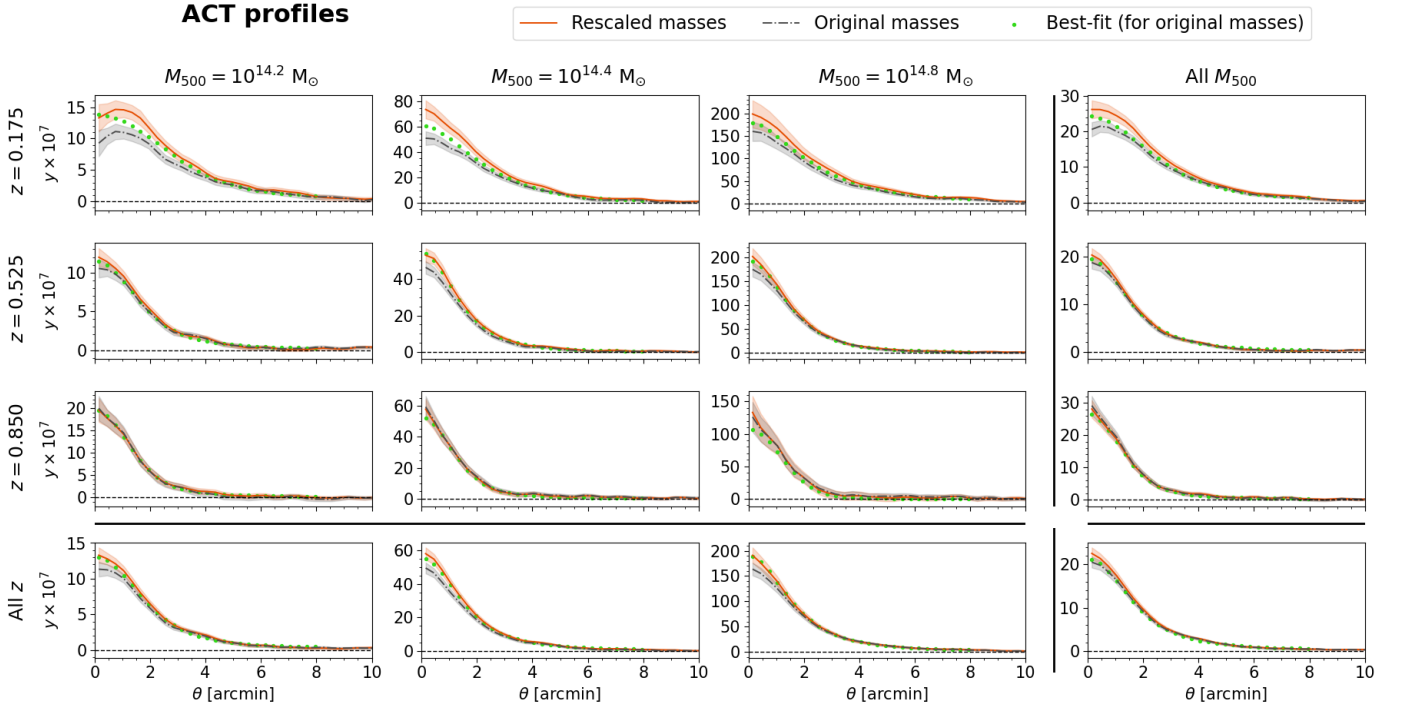


Figure 17. Same as in Fig. 16, but for the profiles measured on the ACT map. The profiles obtained with the fiducial sample are this time plotted in red color.

chose to present and discuss this particular selection of papers to highlight the novel aspects introduced by each of them, namely the systematic application of the UPP to cluster pressure profiles derived from X-ray data (Arnaud et al. 2010), the extension of a similar study to profiles reconstructed from SZ data (Planck Collaboration et al. 2013), considerations on possible mass and redshift dependences of UPP parameters (Sayers et al. 2016), the introduction of ACT data (Pointecouteau et al. 2021) and the importance of the hydrostatic mass bias (He et al. 2021). All of these aspects are also considered in our data analysis and theoretical modeling; the change in the approach from considering a reduced number of clusters to reconstructing the statistical properties of an extended sample, as in Gong et al. (2019), is instead particularly relevant and is then described in the main text in Section 1.

Looking back at Table 1, the best-fit numerical values resulting from these studies show a large scatter. Two main factors contribute to the observed differences. First of all, the UPP parameters are intrinsically degenerate, as it is clear from the functional form in Eq. 3; this implies that different combinations of parameter values can provide equally effective predictions for the observed pressure profiles. A possible way to circumvent this issue, adopted for example by Sayers et al. (2016) and Pointecouteau et al. (2021), is to keep some of the parameters fixed in the analysis, which comes at the price of a slight loss in the generality of the fitted model. In our study we chose, in a more bias-free approach as in Gong et al. (2019), to keep all parameters free, with the exception of the inner slope γ as it is customary in purely SZ-based analyses. Still, we acknowledge that parameter degeneracy is an important issue, and as such it is extensively addressed in our discussion of the fit results in Sections 6.2 and 6.3.

The second main reason for the scatter observed in Table 1 is that, whenever the chosen sample is restricted to a handful of clusters which are well resolved and characterized by observations at different wavelengths, the results on the UPP estimates are inevitably subject to potential selection biases. This is in generally acknowledged in the studies described in this section. In particular, it is worth stressing that cluster samples constructed on the basis of existing high-quality data in ancillary studies are non-representative, which prevents the conclusions from the corresponding studies to be extended to a generic cluster with mass and redshift in the sample span. The only exceptions from the above list are the works based on REXCESS, which is purposely built as a representative sample. The cluster sample used in this work is not only representative (as it in-

cludes all clusters with estimated mass above a common threshold) but also complete (typically $> 90\%$, see Section 3), which is a fundamental difference compared to the previous studies. Possible dependences of the UPP parameters on cluster mass and redshift is actually one of the core topic of our analysis, and is explored by binning our cluster sample in different M_{500} and z bins as detailed in Section 4.1.

B. SYSTEMATIC ERRORS FROM MASS RE-SCALING

We consider an alternative version of our reference cluster sample, obtained by merging KiDS, WHL and DESI only after imposing the lower mass cut $M_{500} > 10^{14} M_{\odot}$, but without applying any mass rescaling to WHL and DESI. We remove cluster repetitions following the same criteria as in Section 3.5, i.e., we always keep KiDS clusters while for the remaining repetitions between WHL and DESI we randomly choose which one to discard. In the end, KiDS, WHL and DESI contribute with 806, 15,114 and 9,684 clusters respectively, for a total of 25,604 clusters spanning again the redshift range $0.02 < z < 0.97$ and the mass range $14.0 < \log(M_{500}/M_{\odot}) < 15.2$. The cluster redshift and mass distributions are qualitatively similar to the ones shown in Fig. 6. We then split the clusters over the same set of M - z bins considered for our fiducial sample, and proceed with the measurement of the stacked signal, the angular profiles and the covariance matrices following the same methodology described in Section 4.2. We do not include plots of the resulting stacks and correlation matrices, as they are similar to the ones already shown for our fiducial sample. Instead, we show a comparison between the measured profiles against the ones from the fiducial sample in Fig. 16 for *Planck* and 17 for ACT. We notice that for the lowest redshift bin there is a clear offset in the profile amplitude; this difference is instead practically negligible for the highest redshift bin, which is mostly dominated by DESI clusters that (for $z > 0.80$) did not undergo any explicit mass rescaling. In general, the difference is also quite mild for the marginalized cases, with the profiles obtained from the full samples showing compatibility over the whole θ range.

As commented in Section 6.1, we perform our MCMC parameter estimation also on this new set of unscaled profiles. The resulting contours are plotted in Figs. 18 to 22, for all M - z bins. These plots are also used to show the posterior distributions obtained with our fiducial sample; given the large number of resulting contours, we include them here in order to keep the main paper text lighter. As already discussed in Section 6.3, in general the contours obtained from the unscaled sam-

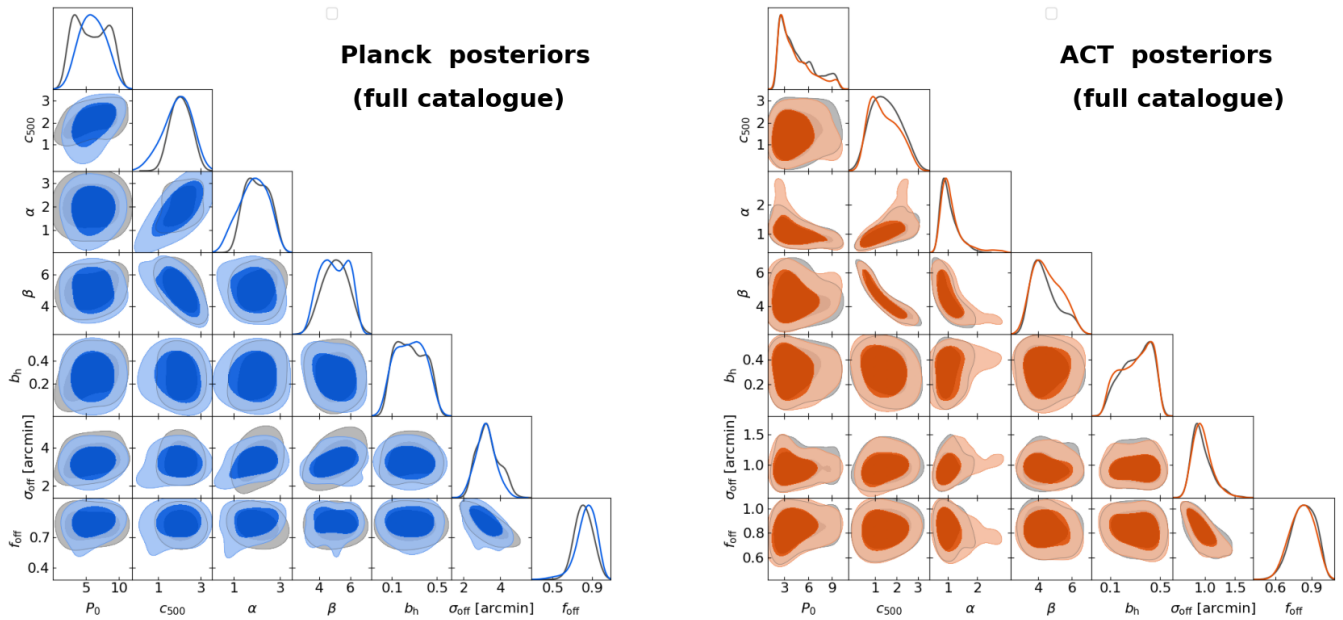


Figure 18. Comparison between the final posteriors (plotted as 68% and 95% C.L. contours) obtained using the cluster sample with and without mass rescaling, for the case of *Planck* (left) and ACT (right). The colored contours were obtained with the mass-rescaled catalog, and are the same as the ones shown in Fig. 12. Gray contours were derived from the catalog obtained with no mass-rescaling.

ple resemble the ones obtained from the fiducial sample; any systematic errors deriving from our mass rescaling are then of second order compared to the final statisti-

cal errors obtained on the parameters, which in turn are mostly driven by the degeneracy of the model.

REFERENCES

- Aghanim, N., Douspis, M., Hurier, G., et al. 2019, *A&A*, 632, A47, doi: [10.1051/0004-6361/201935271](https://doi.org/10.1051/0004-6361/201935271)
- Aguado-Barahona, A., Rubiño-Martín, J. A., Ferragamo, A., et al. 2022, *A&A*, 659, A126, doi: [10.1051/0004-6361/202039980](https://doi.org/10.1051/0004-6361/202039980)
- Aihara, H., Allende Prieto, C., An, D., et al. 2011, *ApJS*, 193, 29, doi: [10.1088/0067-0049/193/2/29](https://doi.org/10.1088/0067-0049/193/2/29)
- Alam, S., Albareti, F. D., Allende Prieto, C., et al. 2015, *ApJS*, 219, 12, doi: [10.1088/0067-0049/219/1/12](https://doi.org/10.1088/0067-0049/219/1/12)
- Allen, S. W., Evrard, A. E., & Mantz, A. B. 2011, *ARA&A*, 49, 409, doi: [10.1146/annurev-astro-081710-102514](https://doi.org/10.1146/annurev-astro-081710-102514)
- Arnaud, M., Pratt, G. W., Piffaretti, R., et al. 2010, *A&A*, 517, A92, doi: [10.1051/0004-6361/200913416](https://doi.org/10.1051/0004-6361/200913416)
- Barnes, D. J., Vogelsberger, M., Pearce, F. A., et al. 2021, *MNRAS*, 506, 2533, doi: [10.1093/mnras/stab1276](https://doi.org/10.1093/mnras/stab1276)
- Battaglia, N., Bond, J. R., Pfrommer, C., & Sievers, J. L. 2012, *ApJ*, 758, 75, doi: [10.1088/0004-637X/758/2/75](https://doi.org/10.1088/0004-637X/758/2/75)
- Bellagamba, F., Roncarelli, M., Maturi, M., & Moscardini, L. 2018, *MNRAS*, 473, 5221, doi: [10.1093/mnras/stx2701](https://doi.org/10.1093/mnras/stx2701)
- Bellagamba, F., Sereno, M., Roncarelli, M., et al. 2019, *MNRAS*, 484, 1598, doi: [10.1093/mnras/stz090](https://doi.org/10.1093/mnras/stz090)
- Birkinshaw, M. 1999, *PhR*, 310, 97, doi: [10.1016/S0370-1573\(98\)00080-5](https://doi.org/10.1016/S0370-1573(98)00080-5)
- Bleem, L. E., Bocquet, S., Stalder, B., et al. 2020, *ApJS*, 247, 25, doi: [10.3847/1538-4365/ab6993](https://doi.org/10.3847/1538-4365/ab6993)
- Böhringer, H., Schuecker, P., Pratt, G. W., et al. 2007, *A&A*, 469, 363, doi: [10.1051/0004-6361:20066740](https://doi.org/10.1051/0004-6361:20066740)
- Carlstrom, J. E., Holder, G. P., & Reese, E. D. 2002, *ARA&A*, 40, 643, doi: [10.1146/annurev.astro.40.060401.093803](https://doi.org/10.1146/annurev.astro.40.060401.093803)
- Czakon, N. G., Sayers, J., Mantz, A., et al. 2015, *ApJ*, 806, 18, doi: [10.1088/0004-637X/806/1/18](https://doi.org/10.1088/0004-637X/806/1/18)
- Davis, M., Efstathiou, G., Frenk, C. S., & White, S. D. M. 1985, *ApJ*, 292, 371, doi: [10.1086/163168](https://doi.org/10.1086/163168)
- de Jong, J. T. A., Verdoes Kleijn, G. A., Erben, T., et al. 2017, *A&A*, 604, A134, doi: [10.1051/0004-6361/201730747](https://doi.org/10.1051/0004-6361/201730747)
- Dey, A., Schlegel, D. J., Lang, D., et al. 2019, *AJ*, 157, 168, doi: [10.3847/1538-3881/ab089d](https://doi.org/10.3847/1538-3881/ab089d)
- Fang, W., Kadota, K., & Takada, M. 2012, *PhRvD*, 85, 023007, doi: [10.1103/PhysRevD.85.023007](https://doi.org/10.1103/PhysRevD.85.023007)

Planck posteriors (independent M-z bins)

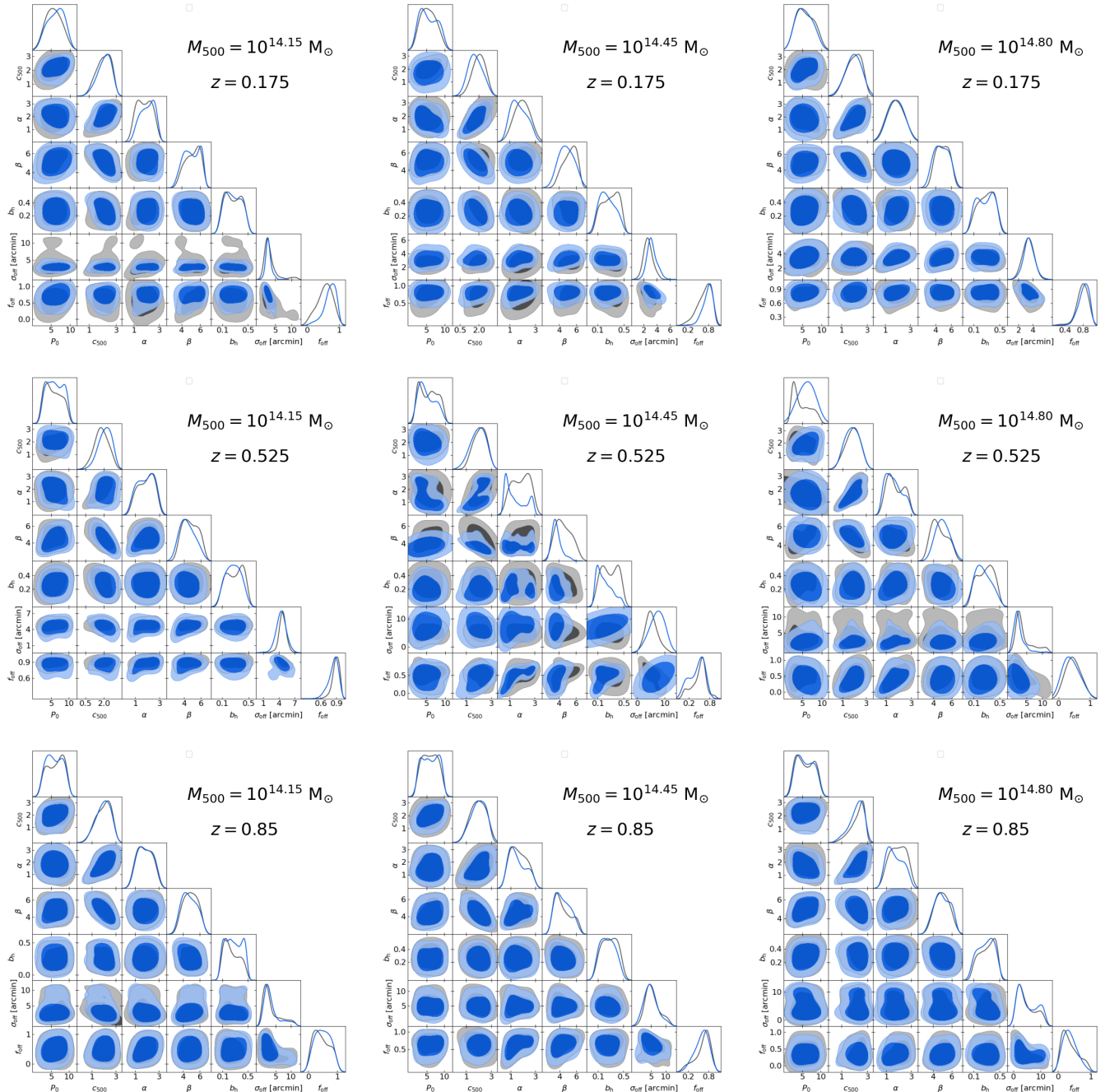


Figure 19. *Planck* posterior distributions (68% and 95% C.L. contours) on the fitted parameters for each independent M - z bin, obtained from the mass-rescaled catalog (blue) and the one with no mass rescaling (gray).

Planck posteriors (marginalized bins)

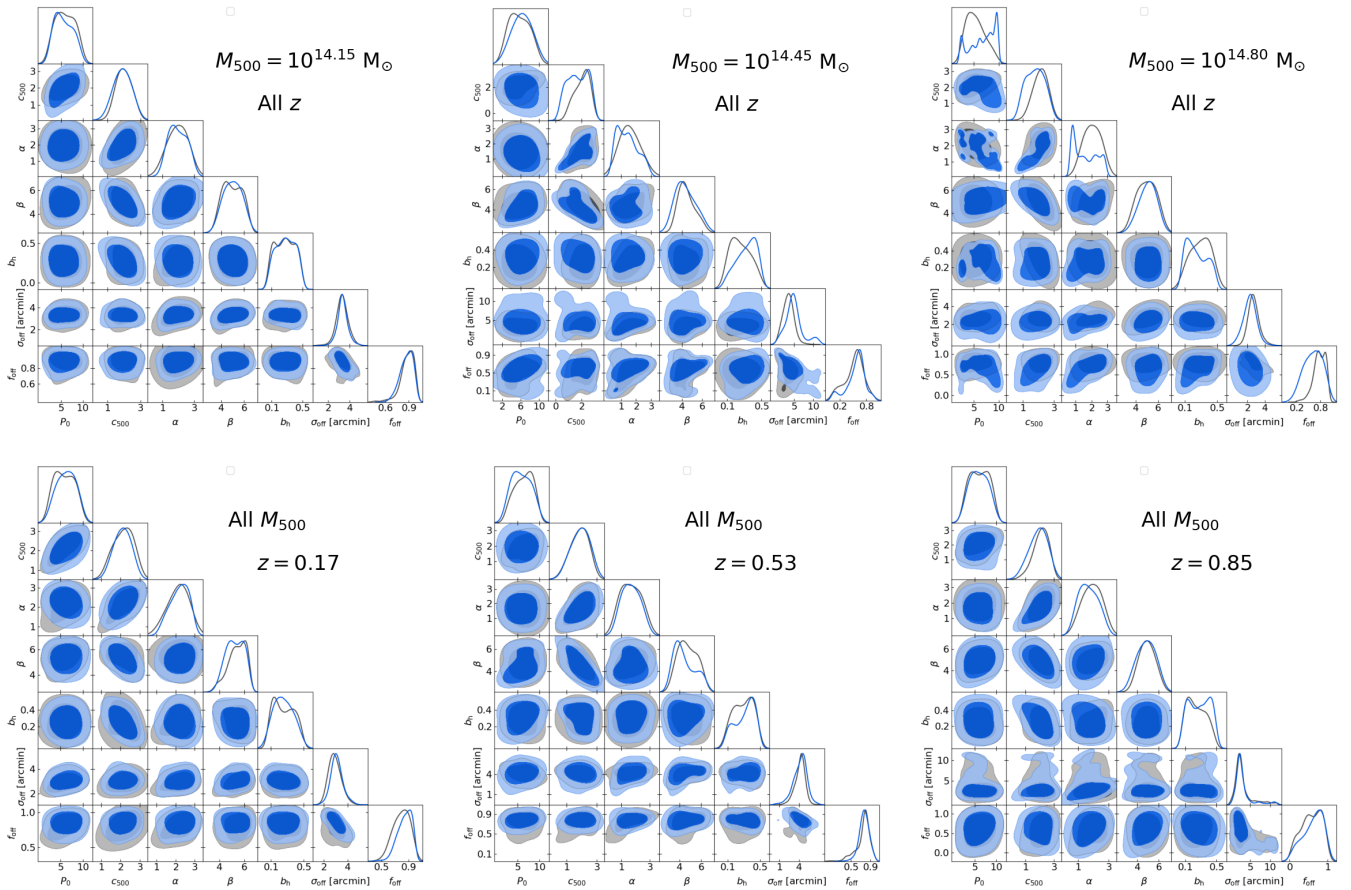


Figure 20. Same as in Fig. 19 but showing this time the bins marginalized over M_{500} or z .

ACT posteriors (independent M-z bins)

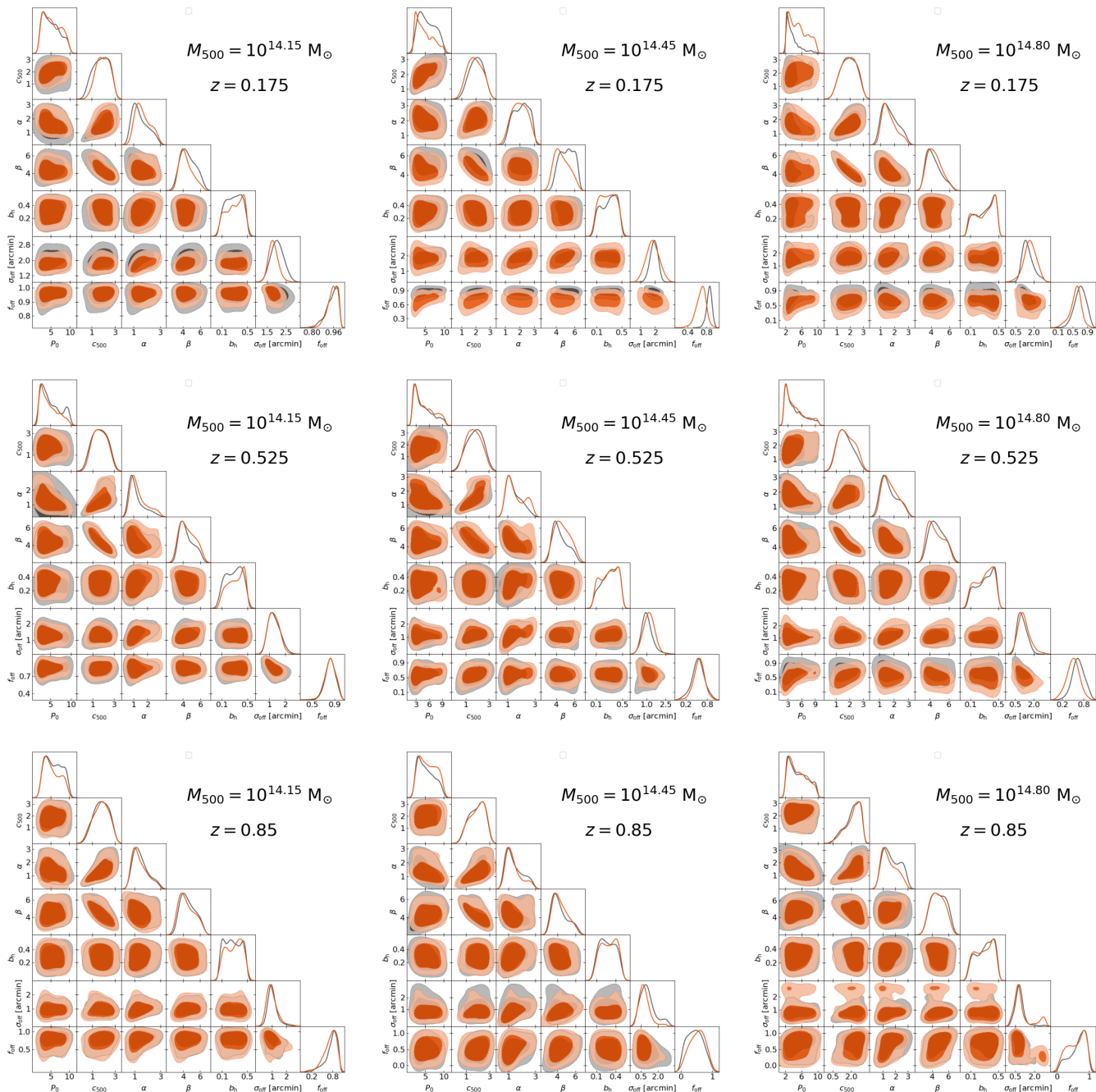


Figure 21. ACT posterior distributions (68% and 95% C.L. contours) on the fitted parameters for each independent M - z bin, obtained from the mass-rescaled catalog (red) and the one with no mass rescaling (gray).

ACT posteriors (marginalized bins)

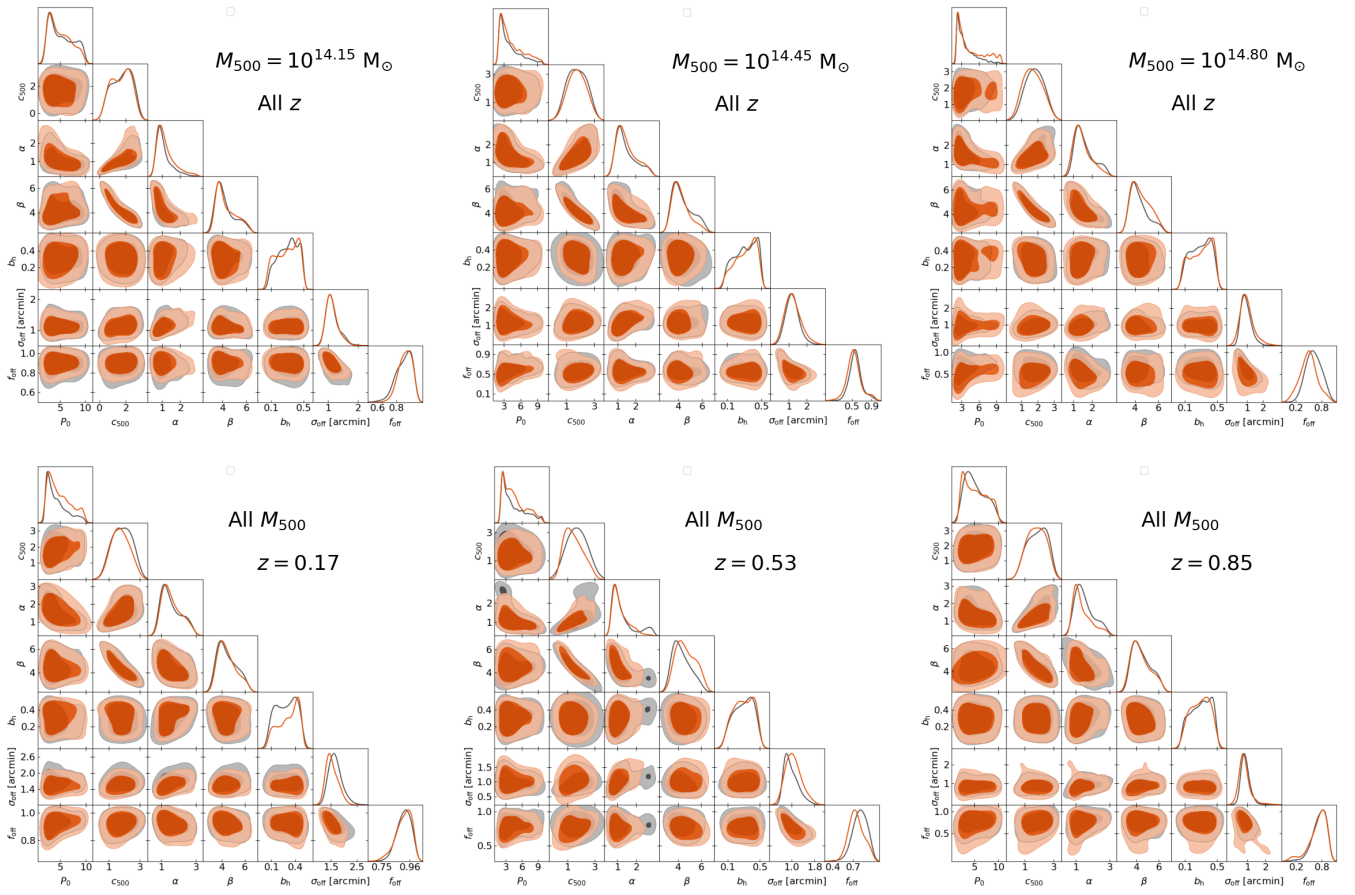


Figure 22. Same as in Fig. 21 but showing this time the bins marginalized over M_{500} or z .

- Ferragamo, A., Barrena, R., Rubiño-Martín, J. A., et al. 2021, *A&A*, 655, A115, doi: [10.1051/0004-6361/202140382](https://doi.org/10.1051/0004-6361/202140382)
- Giocoli, C., Marulli, F., Moscardini, L., et al. 2021, *A&A*, 653, A19, doi: [10.1051/0004-6361/202140795](https://doi.org/10.1051/0004-6361/202140795)
- Gong, Y., Ma, Y.-Z., & Tanimura, H. 2019, *MNRAS*, 486, 4904, doi: [10.1093/mnras/stz1177](https://doi.org/10.1093/mnras/stz1177)
- Goodman, J., & Weare, J. 2010, *Communications in Applied Mathematics and Computational Science*, 5, 65, doi: [10.2140/camcos.2010.5.65](https://doi.org/10.2140/camcos.2010.5.65)
- Górski, K. M., Hivon, E., Banday, A. J., et al. 2005, *ApJ*, 622, 759, doi: [10.1086/427976](https://doi.org/10.1086/427976)
- Hartlap, J., Simon, P., & Schneider, P. 2007, *A&A*, 464, 399, doi: [10.1051/0004-6361:20066170](https://doi.org/10.1051/0004-6361:20066170)
- Hasselfield, M., Hilton, M., Marriage, T. A., et al. 2013, *JCAP*, 2013, 008, doi: [10.1088/1475-7516/2013/07/008](https://doi.org/10.1088/1475-7516/2013/07/008)
- He, Y., Mansfield, P., Rau, M. M., Trac, H., & Battaglia, N. 2021, *ApJ*, 908, 91, doi: [10.3847/1538-4357/abd0ff](https://doi.org/10.3847/1538-4357/abd0ff)
- Hicks, A. K., Ellingson, E., Bautz, M., et al. 2008, *ApJ*, 680, 1022, doi: [10.1086/587682](https://doi.org/10.1086/587682)
- Hilton, M., Sifón, C., Naess, S., et al. 2021, *ApJS*, 253, 3, doi: [10.3847/1538-4365/abd023](https://doi.org/10.3847/1538-4365/abd023)
- Hoekstra, H., Herbonnet, R., Muzzin, A., et al. 2015, *MNRAS*, 449, 685, doi: [10.1093/mnras/stv275](https://doi.org/10.1093/mnras/stv275)
- Hojjati, A., McCarthy, I. G., Harnois-Déraps, J., et al. 2015, *JCAP*, 2015, 047, doi: [10.1088/1475-7516/2015/10/047](https://doi.org/10.1088/1475-7516/2015/10/047)
- Hojjati, A., Tröster, T., Harnois-Déraps, J., et al. 2017, *MNRAS*, 471, 1565, doi: [10.1093/mnras/stx1659](https://doi.org/10.1093/mnras/stx1659)
- Hurier, G., Macías-Pérez, J. F., & Hildebrandt, S. 2013, *A&A*, 558, A118, doi: [10.1051/0004-6361/201321891](https://doi.org/10.1051/0004-6361/201321891)
- Ibitoye, A., Tramonte, D., Ma, Y.-Z., & Dai, W.-M. 2022, arXiv e-prints, arXiv:2206.05689, <https://arxiv.org/abs/2206.05689>
- Ishiyama, T., Prada, F., Klypin, A. A., et al. 2021, *MNRAS*, 506, 4210, doi: [10.1093/mnras/stab1755](https://doi.org/10.1093/mnras/stab1755)
- Joachimi, B., Lin, C. A., Asgari, M., et al. 2021, *A&A*, 646, A129, doi: [10.1051/0004-6361/202038831](https://doi.org/10.1051/0004-6361/202038831)
- Johnston, D. E., Sheldon, E. S., Wechsler, R. H., et al. 2007, arXiv e-prints, arXiv:0709.1159, <https://arxiv.org/abs/0709.1159>
- Klein, M., Oguri, M., Mohr, J. J., et al. 2021, arXiv e-prints, arXiv:2106.14519, <https://arxiv.org/abs/2106.14519>
- Komatsu, E., & Kitayama, T. 1999, *ApJL*, 526, L1, doi: [10.1086/312364](https://doi.org/10.1086/312364)
- Le Brun, A. M. C., McCarthy, I. G., & Melin, J.-B. 2015, *MNRAS*, 451, 3868, doi: [10.1093/mnras/stv1172](https://doi.org/10.1093/mnras/stv1172)
- Ma, Y.-Z., Gong, Y., Tröster, T., & Van Waerbeke, L. 2021, *MNRAS*, 500, 1806, doi: [10.1093/mnras/staa3369](https://doi.org/10.1093/mnras/staa3369)
- Madhavacheril, M. S., Hill, J. C., Naess, S., et al. 2020, *PhRvD*, 102, 023534, doi: [10.1103/PhysRevD.102.023534](https://doi.org/10.1103/PhysRevD.102.023534)
- Makiya, R., Hikage, C., & Komatsu, E. 2020, *PASJ*, 72, 26, doi: [10.1093/pasj/psz147](https://doi.org/10.1093/pasj/psz147)
- Mantz, A., Allen, S. W., Ebeling, H., Rapetti, D., & Drlica-Wagner, A. 2010, *MNRAS*, 406, 1773, doi: [10.1111/j.1365-2966.2010.16993.x](https://doi.org/10.1111/j.1365-2966.2010.16993.x)
- Maturi, M., Bellagamba, F., Radovich, M., et al. 2019, *MNRAS*, 485, 498, doi: [10.1093/mnras/stz294](https://doi.org/10.1093/mnras/stz294)
- Mehrtens, N., Romer, A. K., Hilton, M., et al. 2012, *MNRAS*, 423, 1024, doi: [10.1111/j.1365-2966.2012.20931.x](https://doi.org/10.1111/j.1365-2966.2012.20931.x)
- Nagai, D., Kravtsov, A. V., & Vikhlinin, A. 2007, *ApJ*, 668, 1, doi: [10.1086/521328](https://doi.org/10.1086/521328)
- Navarro, J. F., Frenk, C. S., & White, S. D. M. 1997, *ApJ*, 490, 493, doi: [10.1086/304888](https://doi.org/10.1086/304888)
- Pearce, F. A., Kay, S. T., Barnes, D. J., Bower, R. G., & Schaller, M. 2020, *MNRAS*, 491, 1622, doi: [10.1093/mnras/stz3003](https://doi.org/10.1093/mnras/stz3003)
- Piffaretti, R., Arnaud, M., Pratt, G. W., Pointecouteau, E., & Melin, J. B. 2011, *A&A*, 534, A109, doi: [10.1051/0004-6361/201015377](https://doi.org/10.1051/0004-6361/201015377)
- Planck Collaboration, Ade, P. A. R., Aghanim, N., et al. 2011a, *A&A*, 536, A8, doi: [10.1051/0004-6361/201116459](https://doi.org/10.1051/0004-6361/201116459)
- . 2011b, *A&A*, 536, A11, doi: [10.1051/0004-6361/201116458](https://doi.org/10.1051/0004-6361/201116458)
- . 2013, *A&A*, 550, A131, doi: [10.1051/0004-6361/201220040](https://doi.org/10.1051/0004-6361/201220040)
- . 2016a, *A&A*, 594, A27, doi: [10.1051/0004-6361/201525823](https://doi.org/10.1051/0004-6361/201525823)
- Planck Collaboration, Aghanim, N., Arnaud, M., et al. 2016b, *A&A*, 594, A22, doi: [10.1051/0004-6361/201525826](https://doi.org/10.1051/0004-6361/201525826)
- Planck Collaboration, Aghanim, N., Akrami, Y., et al. 2020, *A&A*, 641, A6, doi: [10.1051/0004-6361/201833910](https://doi.org/10.1051/0004-6361/201833910)
- Pointecouteau, E., Santiago-Bautista, I., Douspis, M., et al. 2021, *A&A*, 651, A73, doi: [10.1051/0004-6361/202040213](https://doi.org/10.1051/0004-6361/202040213)
- Remazeilles, M., Delabrouille, J., & Cardoso, J.-F. 2011, *MNRAS*, 410, 2481, doi: [10.1111/j.1365-2966.2010.17624.x](https://doi.org/10.1111/j.1365-2966.2010.17624.x)
- Rotti, A., Bolliet, B., Chluba, J., & Remazeilles, M. 2021, *MNRAS*, doi: [10.1093/mnras/stab469](https://doi.org/10.1093/mnras/stab469)
- Sarazin, C. L. 1988, *S&T*, 76, 639
- Sayers, J., Golwala, S. R., Ameglio, S., & Pierpaoli, E. 2011, *ApJ*, 728, 39, doi: [10.1088/0004-637X/728/1/39](https://doi.org/10.1088/0004-637X/728/1/39)
- Sayers, J., Golwala, S. R., Mantz, A. B., et al. 2016, *ApJ*, 832, 26, doi: [10.3847/0004-637X/832/1/26](https://doi.org/10.3847/0004-637X/832/1/26)
- Sereno, M., Covone, G., Izzo, L., et al. 2017, *MNRAS*, 472, 1946, doi: [10.1093/mnras/stx2085](https://doi.org/10.1093/mnras/stx2085)

- Sunyaev, R. A., & Zeldovich, Y. B. 1972, *Comments on Astrophysics and Space Physics*, 4, 173
- Takey, A., Schwobe, A., & Lamer, G. 2014, *A&A*, 564, A54, doi: [10.1051/0004-6361/201322973](https://doi.org/10.1051/0004-6361/201322973)
- Tinker, J., Kravtsov, A. V., Klypin, A., et al. 2008, *ApJ*, 688, 709, doi: [10.1086/591439](https://doi.org/10.1086/591439)
- Tinker, J. L., Robertson, B. E., Kravtsov, A. V., et al. 2010, *ApJ*, 724, 878, doi: [10.1088/0004-637X/724/2/878](https://doi.org/10.1088/0004-637X/724/2/878)
- Vikhlinin, A., Burenin, R. A., Ebeling, H., et al. 2009, *ApJ*, 692, 1033, doi: [10.1088/0004-637X/692/2/1033](https://doi.org/10.1088/0004-637X/692/2/1033)
- Voges, W., Aschenbach, B., Boller, T., et al. 1999, *A&A*, 349, 389
- Voit, G. M. 2005, *Reviews of Modern Physics*, 77, 207, doi: [10.1103/RevModPhys.77.207](https://doi.org/10.1103/RevModPhys.77.207)
- von der Linden, A., Allen, M. T., Applegate, D. E., et al. 2014, *MNRAS*, 439, 2, doi: [10.1093/mnras/stt1945](https://doi.org/10.1093/mnras/stt1945)
- Wang, H., Mo, H. J., Yang, X., et al. 2016, *ApJ*, 831, 164, doi: [10.3847/0004-637X/831/2/164](https://doi.org/10.3847/0004-637X/831/2/164)
- Wen, Z. L., & Han, J. L. 2015, *ApJ*, 807, 178, doi: [10.1088/0004-637X/807/2/178](https://doi.org/10.1088/0004-637X/807/2/178)
- Wen, Z. L., Han, J. L., & Liu, F. S. 2012, *ApJS*, 199, 34, doi: [10.1088/0067-0049/199/2/34](https://doi.org/10.1088/0067-0049/199/2/34)
- Yan, Z., Raza, N., Van Waerbeke, L., et al. 2020, *MNRAS*, 493, 1120, doi: [10.1093/mnras/staa295](https://doi.org/10.1093/mnras/staa295)
- Yang, X., Mo, H. J., van den Bosch, F. C., & Jing, Y. P. 2005, *MNRAS*, 356, 1293, doi: [10.1111/j.1365-2966.2005.08560.x](https://doi.org/10.1111/j.1365-2966.2005.08560.x)
- Yang, X., Mo, H. J., van den Bosch, F. C., et al. 2006, *MNRAS*, 373, 1159, doi: [10.1111/j.1365-2966.2006.11091.x](https://doi.org/10.1111/j.1365-2966.2006.11091.x)
- . 2007, *ApJ*, 671, 153, doi: [10.1086/522027](https://doi.org/10.1086/522027)
- Yang, X., Xu, H., He, M., et al. 2021, *ApJ*, 909, 143, doi: [10.3847/1538-4357/abddb2](https://doi.org/10.3847/1538-4357/abddb2)